THE USE OF ALLOY ANODES AND CONVENTIONAL ELECTROLYTES IN MAGNESIUM BATTERIES

by

Tuan T. Tran

Submitted in partial fulfilment of the requirements
for the degree of Master of Science

at

Dalhousie University
Halifax, Nova Scotia
December 2012

DALHOUSIE UNIVERSITY

DEPARTMENT OF CHEMISTRY

The undersigned hereby certify that they have read and recommend to the Faculty of Graduate Studies for acceptance a thesis entitled "THE USE OF ALLOY ANODES AND CONVENTIONAL ELECTROLYTES IN MAGNESIUM BATTERIES" by Tuan T. Tran in partial fulfilment of the requirements for the degree of Master of Science.

Dated: December 10th, 2012

Supervisor: _____

Readers: _____

_____

_____

DALHOUSIE UNIVERSITY

DATE: December 10th, 2012

AUTHOR: Tuan T. Tran

TITLE: The Use of Alloy Anodes and Conventional Electrolytes in Magnesium Batteries

DEPARTMENT OR SCHOOL: Department of Chemistry

DEGREE: MSc CONVOCATION: May YEAR: 2013

_____

Signature of Author

TABLE OF CONTENTS

LIST OF TABLES

LIST OF FIGURES

ABSTRACT

Magnesium-based batteries are promising for use in future electrified vehicles and electrical power grids due to their high theoretical volumetric energy. However, there exist many challenges in the development of electrode materials, electrolytes and even cell hardware. In this thesis, the use of alloy-based anodes and conventional electrolytes in Mg batteries is described. Mg(bis(trifluoromethanesulfonyl)imide)$_2$ salt in acetonitrile electrolytes were found to have utility in Mg-ion batteries; however, this electrolyte could not be used in Mg metal batteries, since Mg plating could not be supported. Alloy-based electrodes were found to have high theoretical volumetric capacities in Mg batteries. Experiments showed that a lead (Pb) anode could be cycled reversibly in a Mg cell and has potential for use as an anode material for future Mg-ion batteries. Finally, new cell hardware was developed to enable future studies of Mg-ion battery materials and electrolytes at elevated temperatures.

LIST OF ABBREVIATIONS USED

AEC	All-ethyl-complex
AN	Acetonitrile
BMF	Polypropylene blown microfiber separator
DEC	Diethyl carbonate
EC	Ethylene carbonate
FEC	Fluoroethylene carbonate
HDPE	High-density polyethylene
MCMB	Mesocarbon microbeads
TFSI	bis(trifluoromethanesulfonyl)imide
NMC	Lithium nickel manganese cobalt oxide
NMP	N-methylpyrrolidone
PC	Propylene carbonate
PI	polyimide
PVDF	Polyvinylidene difluoride
THF	Tetrahydrofuran
XRD	X-ray diffraction

ACKNOWLEDGEMENTS

I want to use this page to express my gratitude to everyone who has supported me throughout my degree.

Dr. Mark Obrovac, my supervisor, has distributed his interests in battery research to me. Dr. Jeff Dahn, who has been very kind to let me freely access to the facilities in his laboratory. I am very thankful for both of them for teaching me the first lessons on battery's materials, and for all of their valuable advices whenever I got stuck in my research. Thank you very much!

I thank my supervisory members, Dr. Mary Anne White and Dr. Heather Andreas for their guides to make this thesis much better compared to the first draft. In addition to my supervisory members, I also want to thank Dr. Norman Schepp for his kindness on accepting to be the chair of my defence in a very short notice. All of these supports have helped me to complete this thesis on time.

I also want to thank: Dr. Timothy Hatchard and Dr. Robbie Sanderson for help with the combinatory sputtering system; Patricia Scallion for SEM work; Simon Trussler, Kevin Borgel and John Noddin for their help with machining. And all the members of Obrovac's groups for giving me a lot of fun and crazy times while being a member of this group. Thank all of you a lots!

Tuan Tran
December 2012

CHAPTER 1
INTRODUCTION

The rapid increase in oil price due to the depletion of oil reserves affects both the economy and people's daily life. In addition, car exhaust, one of the main causes of global warming, is showing serious impacts on humankind today. Reducing the use of private transportation by using car pools or public transportation, for example, is a temporary solution for these crises. For a long term solution, alternative energy sources which are less expensive and more environmental friendly are needed. As a result, inexpensive electrified vehicles would be highly desirable. The replacement of conventional gasoline engines by electrical engines, thus, requires new type of "fuel" storage device. This makes the search for inexpensive high energy density batteries is an important endeavour.

1.1 Background on Secondary Metal-ion Batteries

Lithium-ion (Li-ion) batteries currently are the highest energy density secondary battery available for mass consumer use. Theoretically, lithium metal is an ideal anode material with the highest specific energy density. This is because lithium has a low molar mass and is highly electropositive. However, alternatively plating and stripping of metallic lithium was found to be problematic in the case of lithium metal secondary batteries [1]. The plating and stripping process was found to be inefficient, requiring a large excess of lithium metal to be used to maintain cycle life [1]. Repeated stripping and plating of a lithium metal electrode also can result in the formation of metal dendrites and high surface area porous deposits, which have an increased reactivity with respect to the

electrolyte [1]. To avoid problems associated with plating and stripping a metal electrode, Li-ion batteries were introduced by Sony in 1992.

In Li-ion batteries, lithium ions are the main charge carriers. A battery contains one or more electrochemical cells in series or in parallel. An electrochemical cell consists of a positive electrode (cathode), a negative electrode (anode), current collectors, separators, ion conducting electrolyte and a cell can. Both electrodes of a Li-ion electrochemical cell are, generally, made from host materials for lithium ions. Hence, without using a lithium metal electrode, Li-ion batteries avoid altogether the problems associated with plating and stripping of metal during cycling. In this thesis, the term "battery" and "cell" will be used interchangeably.

In a Li-ion cell, the positive electrode contains lithium when synthesized, and has low chemical potential with lithium. Meanwhile, the negative electrode has high chemical potential with lithium. Therefore, Li-ion batteries must be first charged after cell construction. During charging, an external voltage is applied. This external voltage provides a rich electron environment in the negative electrode of the battery. Hence, lithium ions, which are oxidized at the positive electrode, will internally travel to the negative electrode. When in use, due to the lower chemical potential at the positive electrode, lithium ions thermodynamically prefer to leave the negative electrode and move to the positive electrode where they will be reduced. As a result electrons are released from the negative electrode and travel to the positive electrode to balance the charge, creating an external current.

Currently, most electrodes for Li-ion cells are made from materials containing layers or tunnels, where lithium ions can be freely intercalated (inserted) or de-

intercalated (extracted) without changing the structure of the host. A relatively small number of commercial cells made by Sony contain an anode comprising a tin alloy in which lithium can be reversibly electrochemically alloyed and de-alloyed [2]. Due to the ability of intercalation and de-intercalation of lithium ions to/from the anode and cathode, Li-ion batteries can be reversibly charged and discharged many times.

1.2 Motivation

1.2.1 New Directions in Battery Research

Two decades after their introduction, the development of Li-ion battery has reached an advanced state. Recently, this type of battery is being utilized for energy storage in electrified vehicles by many automobile manufacturers, such as Toyota (Prius), Chevrolet (Volt), Nissan (Leaf) and Tesla (model S). However, several disadvantages, such as higher price, shorter operating distance, and longer "refill" (recharge) time of these electrified vehicles compared to gasoline vehicles prevent them from being commonly used. Amongst these disadvantages, cost and shorter driving range seems to be the biggest drawbacks of the fully electrified vehicles. In order to overcome these problems, batteries with lower cost and further energy density improvements are needed. Fortunately, as energy density is increased, cost per unit energy tends to be reduced, as the same amount of material can produce more energy. Therefore reducing cost can be achieved somewhat by increasing the energy density. The solutions for these problems should not only be limited to lithium-ion battery materials, but altogether new high energy battery chemistries should be included in this search. For instance, volumetrically, magnesium batteries can theoretically have higher energy density than lithium batteries in a number of cell chemistries. Therefore, batteries based on electropositive metals other

than lithium, such as sodium [3-6] and magnesium [7-8], are currently receiving greater research interest as alternatives to Li-ion batteries.

There is a great potential to increase anode energy densities in Li-ion cells by using alloy materials [9]. Such alloys have higher energy density than graphite, but suffer from large volume changes during lithium insertion, making their implementation more difficult [9]. Nevertheless, these issues can be overcome with a combination of alloy, electrolyte and electrode design. As a result, alloy-based anode materials are likely to be utilized in the next generation of high energy density Li-ion batteries.

According to binary alloy phase diagrams, electropositive metals such as sodium, potassium, magnesium, calcium and aluminum have a similar alloying chemistry to lithium, since they all form alloys with similar host metals (Si, Sn, Al, Bi, Pb, etc.). Therefore, it might be possible to form these alloys electrochemically, making alloys a possible negative electrode host material for electropositive metal ion cells. Moreover, the doubly and triply-charged metal alloys are predicted to have a greater energy density than any lithium negative electrode known and operate at potentials at which organic electrolytes are known to be stable. This provides an opportunity for the development of cell chemistries with higher energy density and higher thermal stability than lithium ion technology. Therefore, it is important to determine if such alloys will be practical as negative electrodes in metal-ion cells in order to validate future research in this area.

1.2.2 Advantages for Mg-Based Batteries

As mentioned in the previous section, alternative metal-ion batteries show promising directions for the development of high capacity cells in the future. In order to narrow this research to the most interesting direction, Chapter 2 describes a theoretical

study of alloy-based anode materials in many different metal-ion systems, where the active metal ions of interest (A) are those that are highly electropositive: A = Na, K, Ca, Mg, and Al. If a metal M is used as a host alloy for these active metals, the results from Chapter 2 clearly shows that the doubly and triply charged A_xM alloys all have greater volumetric energy densities than conventional graphite anodes in Li-ion cells (Figure 1). In particular, Mg_xM and Al_xM alloys have as great or greater energy density than even Li_xM alloys. Between these two metals, the Al-ion system is extremely attractive. However, no work to date has been published on this system and reversible electrochemistry at room temperatures may not be possible. On the other hand, magnesium batteries with good reversibility at room temperature have been reported [10]. Therefore in this work, magnesium-based batteries have higher priority.

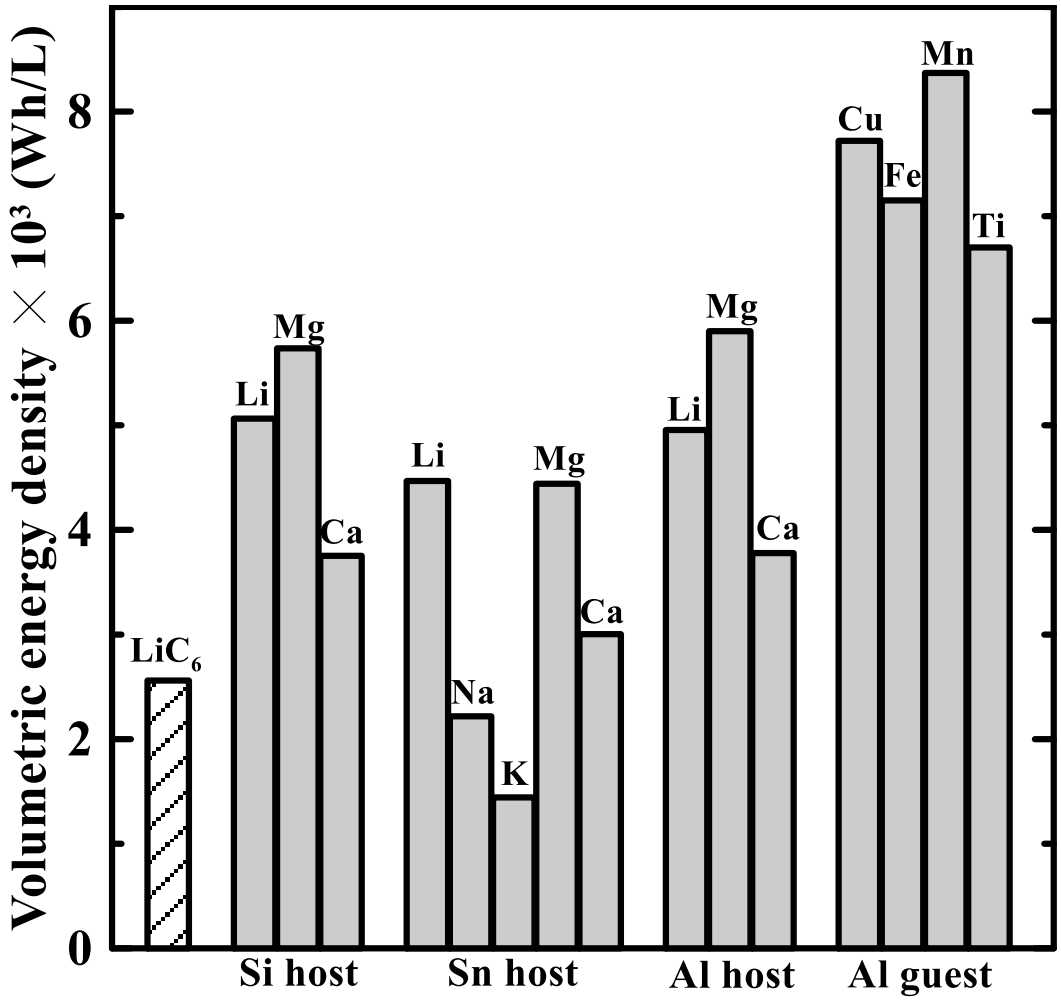

Figure 1 – The volumetric energy density of A_xM alloys versus a 3.75 V (vs. Li) cathode. The volumetric energy density of a conventional graphite negative electrode material for a lithium ion battery is shown for comparison.*

Additionally to the potential to offer a high energy density battery, metallic magnesium is low in cost, high abundant [11] and requires a similar amount of energy to refine as lithium. According to the studies conducted by the U.S. Geological Survey agent (USGS) in 1998, the cost for metallic Mg is about 27 times less expensive than metallic Li: $3.50 USD/kg of Mg (equivalent to 0.0016 USD/Ah) [12] and $95 USD/kg of Li (equivalent to 0.025 USD/Ah) [13]. In terms of the environmental impact on

* Reproduced following the same calculations described in T.T. Tran and M.N. Obrovac, *J. Electrochem. Soc.*, **158** (2011) A1411.

mining these metals, the electrolysis process to obtain metallic lithium requires about 700 MJ of energy to produce 1 kg of metallic Li [14]. Meanwhile, metallic Mg is commonly produced using Pidgeon process (Reaction 1) and requires 355 MJ of energy to obtain 1 kg of metallic Mg [15]. This corresponds to a comparable energy required to produce these metals of 4860 kJ and 4310 kJ per Faraday of charge in a battery, for metallic Li and Mg, respectively.

$$2MgO_{(s)} + Si_{(s)} \xrightarrow{high\ T} 2Mg_{(g)} + SiO_{2(s)}$$

Reaction 1 – Pidgeon reaction for the production of metallic Mg.

With the current technology of Li-ion batteries, lithium carbonate (Li_2CO_3) has replaced metallic Li as the raw material in synthesis process of electrodes; it helps to reduce the environmental impact on mining to about 30 MJ of non-renewable energy for 1 kg of Li_2CO_3 [16]. The comparable information has not been yet available in the case of Mg-ion batteries, since the final chemistry of Mg batteries is not known. However, further development of Mg-ion batteries can be foreseen to decrease the environmental impact on mining raw materials if a similar material such as magnesite ($MgCO_3$) was used to replace Mg metal. From this analysis it is seen that Mg is a low cost, highly abundant resource on which to base battery chemistries. In addition, Mg is air stable, which is likely to lower the cost of Mg metal based batteries compared to that of Li metal batteries of the past.

1.2.3 The Direction of This Research

One of the biggest challenges for the development of practical Mg-based batteries is the development of a practical electrolyte. It has long been known that Mg can be deposited from Grignard reagents electrolytes at low overpotentials [17]. However, these

electrolytes are flammable, toxic, unstable and reactive in air; thus, the practicality of such electrolytes is questionable. Recently, reversible cycling of a Bi vs. Mg cell has been reported in an electrolyte composed of $Mg[N(SO_2CF_3)_2]_2$ (or magnesium di-bis(trifluoromethane sulfonyl)imide, abbreviated here as $Mg(TFSI)_2$) in acetonitrile (AN) [18]. However, acetonitrile is known to be reductively unstable and electrolytes containing TFSI salts are known to be corrosive towards aluminum cell parts when used in lithium ion cells [19]. These could lead to potential issues for the use of this electrolyte in practical Mg cells. Therefore, in Chapter 3, a detailed study of the use of $Mg(TFSI)_2$/AN electrolyte for Mg-based batteries is presented in order to examine the practicality of this electrolyte.

As mentioned above, Mg can be reversibly deposited from Grignard reagents at low overpotentials [17]. In fact, up until now, this is the only non-aqueous electrolyte that is well-known for this property at room temperature. While waiting for more practical electrolytes to be discovered, alternative materials for Mg metal that can be used as the counter electrode for the research on electrode's materials and electrolytes for Mg-based batteries can still be developed. Using the theoretical method that will be described in Chapter 2, magnesiated lead (Mg_xPb, where $0 < x < 2$) with the predicted potential of as low as 0.10 V vs. Mg is a strong candidate to replace Mg metal as the counter electrode. A more detail study on magnesiated lead will be shown in Chapter 4 of this thesis.

Chapter 5 introduces newly designed cell hardware. As learned from the experiments described in Chapter 3 and Chapter 4, the development of materials for Mg-based batteries usually requires using highly reactive electrolytes, elevated operating temperatures and three electrode cells. As a result, a more rigid cell design that can

enable research in these conditions is needed. Here, a cell has been developed especially for this type of research.

Finally, Chapter 6 is an overview for the whole thesis. Suggestions for future work in order to complete the discussed projects are provided.

CHAPTER 2
THEORETICAL STUDY OF ALLOY MATERIALS FOR NEGATIVE ELECTRODE IN METAL-ION BATTERIES[†]

2.1 Introduction

2.1.1 Previous Study of Alloy Materials for Negative Electrode in Lithium-ion Batteries

In a recent study, the volume of alloy host materials is shown to increase significantly as lithium is inserted [9]. The expansion of such materials follows Vegard's law, the alloy composition has linear relationships to its volume during lithium insertion. In fact, it was found that lithium occupies the same volume (9 ml/mol) in all alloy host materials [9]. This simple relationship between lithium content and volume allowed for a theory to be developed for the design of alloy materials to provide high energy density negative electrodes for Li-ion batteries.

2.1.2 Hypothesis for The Volume Expansion of Alloy Systems for Different Metal-ion Batteries

In reference [9], the volume of Li_xM alloys shown to follow a simple linear relation:

$$V = xk + v_o \tag{1}$$

[†] Materials from this chapter were used with permission from T.T. Tran and M.N. Obrovac, *J. Electrochem. Soc.*, **158** (2011) A1411. T.T. Tran's contribution to this publication was the calculation of theoretical alloy voltages, volume expansions and energy densities as well as co-authoring the manuscript text.

where V is the molar volume of the Li_xM alloy per metal M, v_o is the molar volume of pure metal M and k is the molar volume of lithium in the Li_xM alloy. Equation (1) is simply a reformulation of Vegard's law.

It is simple to extend this theory to the more general case of A_xM alloys where the guest ion, A^{z+}, has a charge, z, that can be greater than one. Analogous to equation (1), according to Vegard's law, the volume of an alloy A_xM per host metal atom M per unit charge stored in the alloy is predicted as:

$$V = xzk_A + v_o \tag{2}$$

where k_A is now the volume occupied per unit charge stored in the A_xM alloy. In the case of Li, z = 1 and equation (2) becomes identical to equation (1).

In this chapter, the volume changes that occur when different electropositive metals (Na, K, Mg, Ca and Al) are inserted in alloy hosts and their predicted volumetric energy density will be studied. It shows that the volume expansion of these systems also follow the Vegard's law as described in equation (2). Additionally, a method, which is used to calculate the energy density of these alloy systems, will be introduced. From these energy density's predictions, the most interested system can be chosen for the future high density energy batteries.

2.2 Experimental

Anodes for electrochemical measurements consisted of 6:2:2 active metal:carbon black (Super-P, Timcal, Switzerland):polyimide binder (PI2555, HD MicroSystems) by volume. The electrodes were cycled in coin cells versus a lithium metal anode at a C/20 rate using an electrolyte of 1 M $LiPF_6$ in 4:2:4 fluoroethylene carbonate (FEC):ethylene

carbonate (EC):diethyl carbonate (DEC) by volume. All solvents were used as received from Novolyte Technologies.

2.3 Results

2.3.1 Alloy Materials and Their Volume Expansion

Figure 2 shows a plot of the volume per mole of host atom of the stable binary A_xSn phases at room temperature, plotted versus the charge stored per host atom (xz). The stable phases plotted were those that exist at room temperature according to the equilibrium phase diagram of the A-Sn systems (where A = Li [20], Na [21], K [22], Ca [23], and Mg [24]). Molar volumes were derived from the crystallographic volume of each phase [25]. Calculated data points on Figure 2 are based on the information available on both the phase diagrams and the crystallographic volume. As predicted by equation (2), the volume of the alloy per host metal increases linearly with the amount of charge stored in the alloy. The increase in volume per unit charge, k_A, is the greatest for large singly charged ion, but is much smaller for doubly charged ions. Thus, even though Ca^{2+} is a bigger ion than Li^+, the amount of charge stored per unit volume in Sn is nearly the same for Ca_xSn alloys as it is for Li_xSn alloys. Interestingly, Mg_xSn alloys are predicted to store more charge per unit volume than Sn-based negative electrodes for Li-ion batteries.

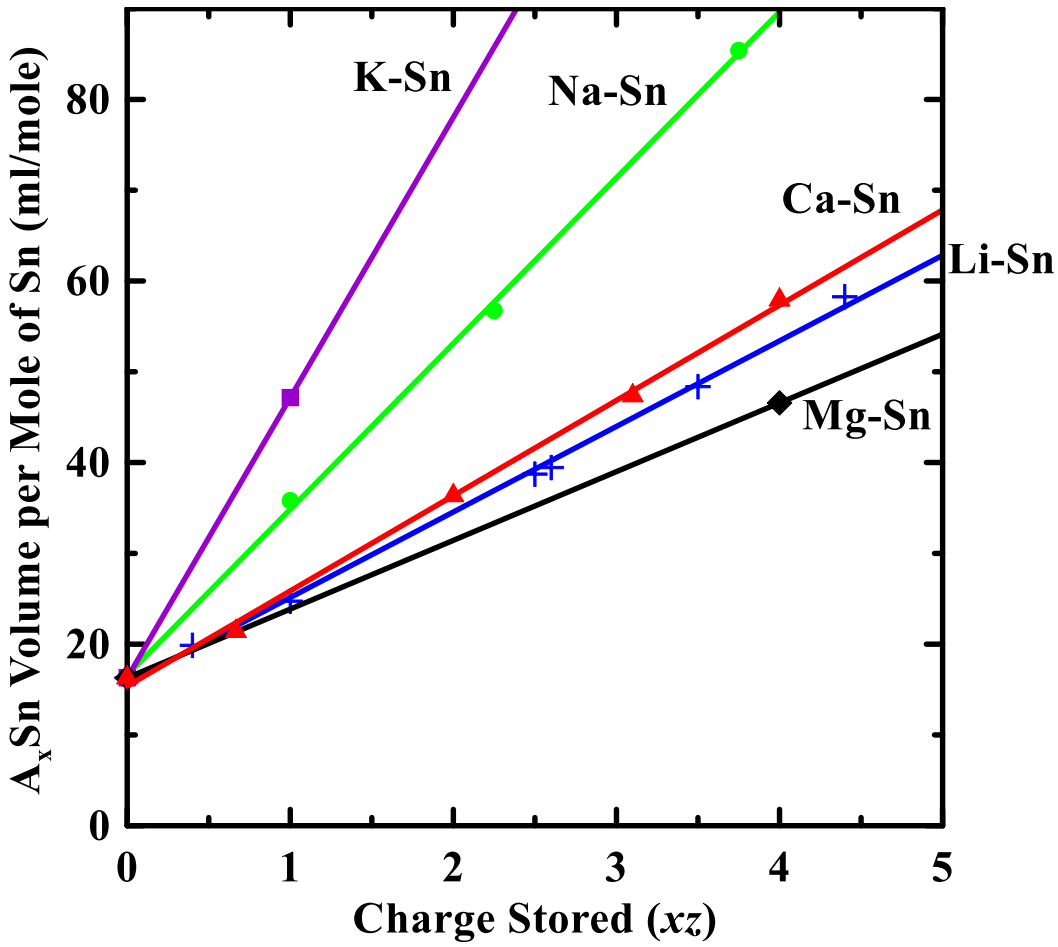

Figure 2 – The molar volume of Sn in A_xSn alloys plotted as a function of the charge stored (*xz*).

Figure 3 shows a plot of the volume per mole of host atom of the stable binary A_xSi phases at room temperature plotted versus the charge stored per host atom (where A = Li [26], Ca [27], and Mg [28]), excepting the $Li_{15}Si_4$ phase, which has been shown to be the highest Li_xSi lithiated phase obtainable at room temperature [29-30]. The behaviour is similar for the case of A_xSn alloys: the volume change per unit charge is less for doubly charged cations. Again, Mg_xSi alloys exceed the volumetric capacity and have less volume expansion per unit charge than the analogous Li_xSi alloys, while Ca_xSi alloys have nearly identical volumetric capacities and volume expansion as the Li_xSi alloys.

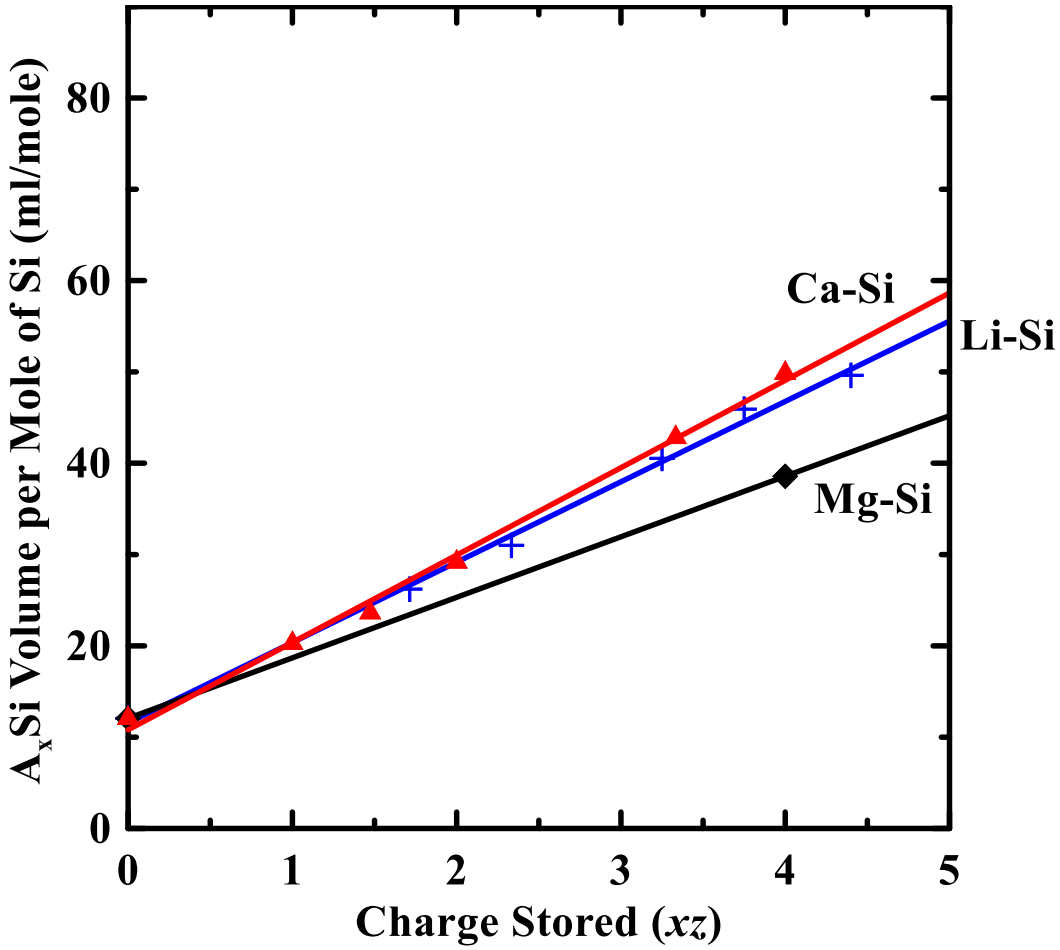

Figure 3 – The molar volume of Si in A_xSi alloys plotted as a function of the charge stored (xz).

Figure 4 shows a plot of the volume per mole of host atom of the stable binary A_xAl phases at room temperature (where A = Li [31], Ca [32], and Mg [33]), plotted versus the charge stored per host atom. The behaviour in the A_xAl system is again very similar to the A_xSi and A_xSn sytems with Li_XAl and Ca_xAl alloys having about the same volumetric capacity and Mg_xAl alloys having a greater volumetric capacity than either.

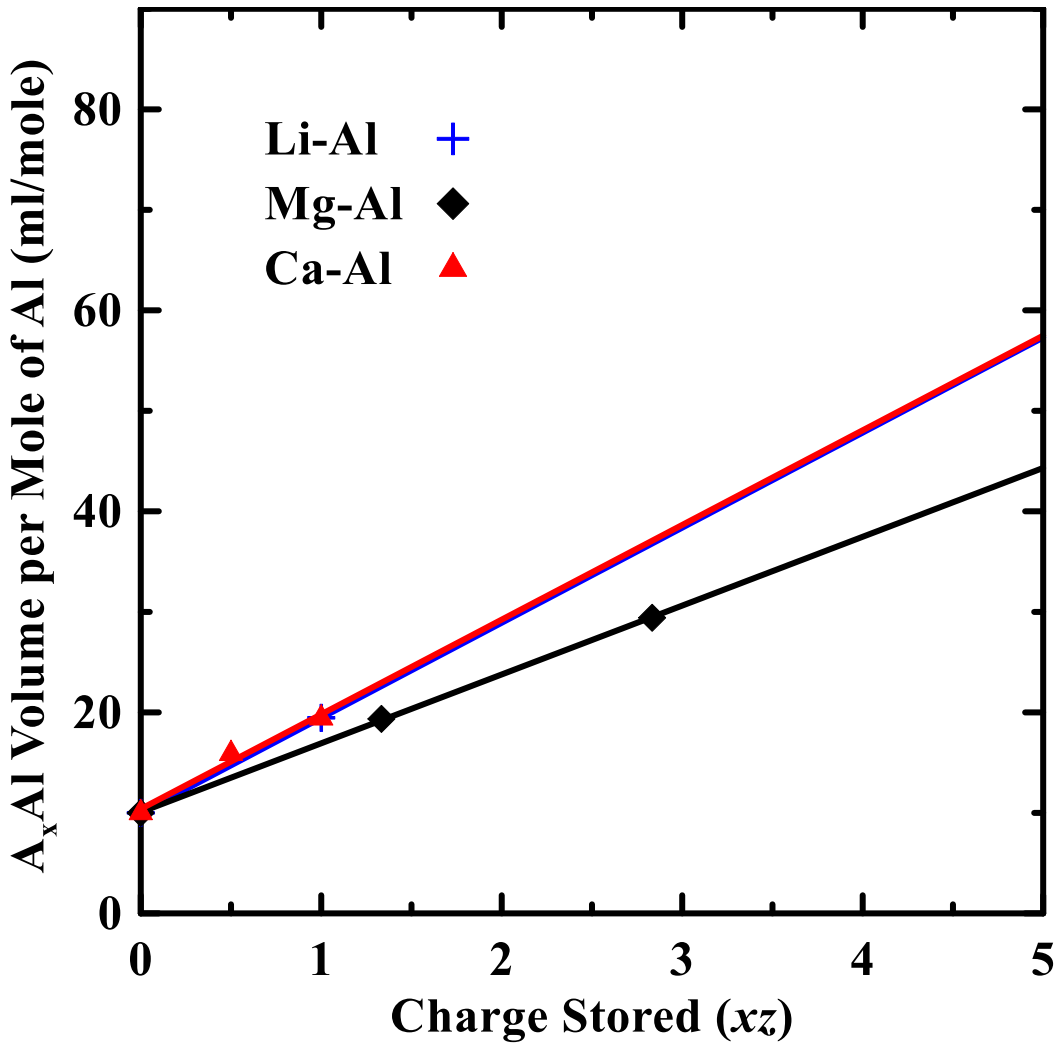

Figure 4 – The molar volume of Al in A_xAl alloys plotted as a function of the charge stored (*xz*).

Aluminum can also be considered as an electropositive triply charged guest ion in which an Al-ion battery can be based. In this case a negative electrode based on a metallic host that forms Al_xM alloys during cell charging can be envisioned. Unlike alkali and alkaline earth metals, aluminum does not form alloys with Si or Sn, but does form alloys readily with transition metals. Because of this, transition metals might be viable elements in which to base negative electrode materials for Al-ion cells. Figure 5 shows a plot of the volume per mole of host atom of the stable binary Al_xM phases (M =

Cu [34], Fe [35], Ti [36], and Mn [37]) at room temperature. Similar to the alkali and alkaline earth metals, the k_A values for Al are nearly the same in all the metal hosts shown.

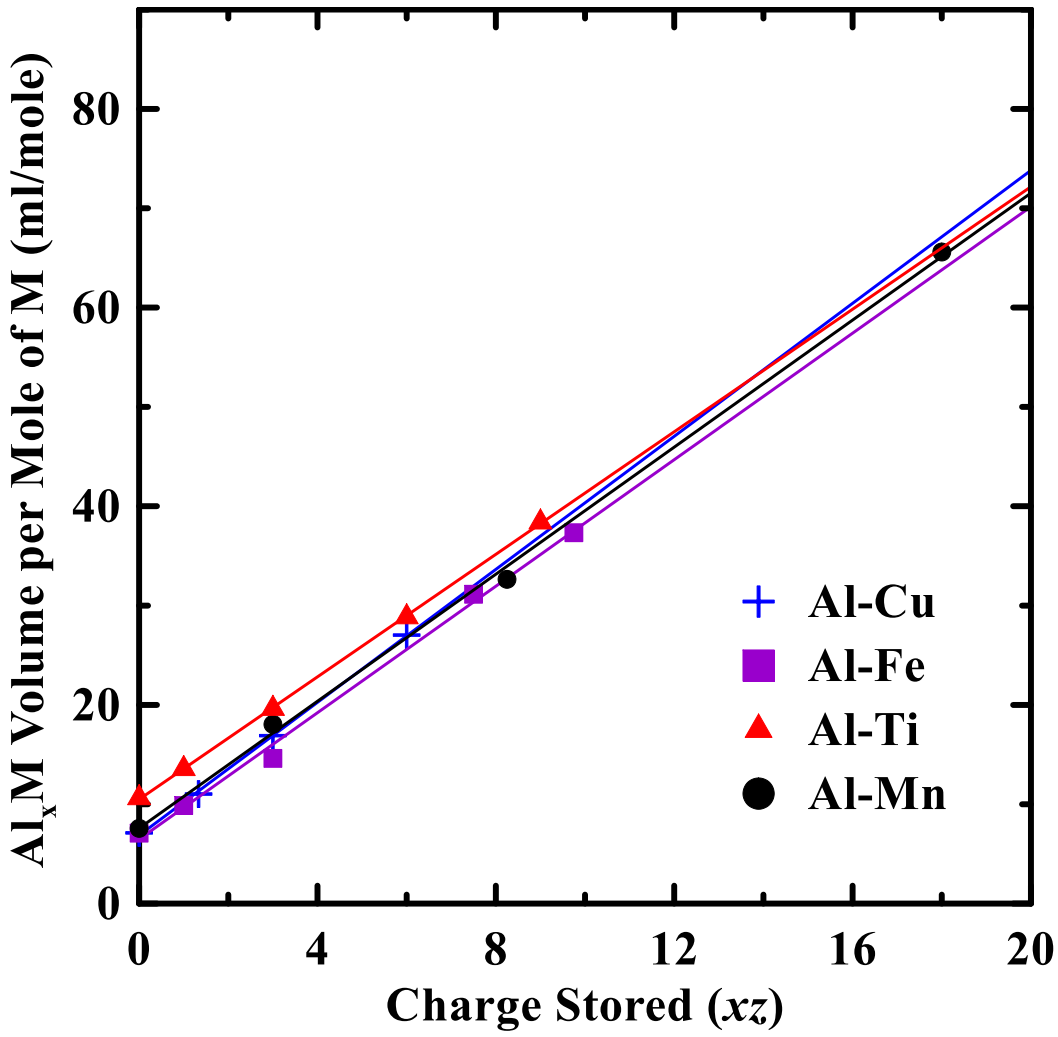

Figure 5 – The molar volume of M in Al_xM alloys plotted as a function of the charge stored (zx).

In a summary for the volume change for alloys that are shown on Figure 1 - 5, Table 1 lists the values of k_A and the volume expansion at fully charge for all metal-host pairs. As can be seen from the figures and Table 1, each guest ion has a characteristic slope, or k_A value, which is nearly the same regardless of the host atom.

Table 1 – Percent volume expansion and k_A listed for various A_xM alloys.

A_xM System	A_xM Phase at Full State of Charge	Volume Expansion at Full State of Charge	k_A (mL $mol^{-1}charge^{-1}$)
Li_xSn	LiSn	52	8.42
Li_xSi	$Li_{15}Si_4$	281	9.02
Li_xAl	LiAl	95	9.46
Na_xSn	$Na_{15}Sn_4$	424	18.26
K_xSn	KSn	190	30.87
Mg_xSn	Mg_2Sn	186	7.57
Mg_xSi	Mg_2Si	220	6.63
Mg_xAl	$Mg_{17}Al_{12}$	194	6.85
Ca_xSn	Ca_2Sn	256	10.49
Ca_xSi	Ca_2Si	313	9.57
Ca_xAl	$CaAl_2$	94	9.42
Al_xTi	Al_3Ti	261	3.08
Al_xMn	Al_6Mn	766	3.20
Al_xFe	$Al_{13}Fe_4$	426	3.18
Al_xCu	Al_2Cu	280	3.35

Table 2 lists the average value of k_A for each guest atom, which can be interpreted as the average molar volume of the guest atom per unit charge in A_xM alloys. Large values of k_A indicate large volume expansion will occur for alloys with host metal ion A. According to this table, the average value of k_A for Al is much less than for other electropositive metals (nearly three times less than Li), indicating that an Al_xM electrode

would have significantly higher capacity and less volume expansion than alloy negative electrodes for alkali and alkaline earth metal ions.

Table 2 - Average k_A values for different metal guest atoms

A in A_xM	k_A (ml mol^{-1} $charge^{-1}$)
Li	9.0 ± 0.5
Na	18.3
K	30.9
Mg	7.0 ± 0.5
Ca	9.8 ± 0.6
Al	3.2 ± 0.1

2.3.2 Alloy Materials and The Volumetric Capacity

In order to evaluate the usefulness of A_xM electrodes in metal ion cells, it is necessary to calculate their theoretical energy density. Here the volumetric energy density is calculated. The volumetric energy density a battery is the most important parameter for applications in consumer electronics [9] and is also a crucial design parameter in automotive applications [38]. Therefore, a volumetric energy density comparison of A_xM alloys is an important indicator for practical applications.

Using equation (2), the volumetric energy density of an A_xM alloy, $\tilde{U}_f$, can be derived:

$$\tilde{U}_f = FV_{avg}\left(\frac{x_f z}{v_o + k_A x_f z}\right) \quad (3)$$

where F = 26.802 Ah/mol is Faraday's constant, x_f is the value of x in the fully occupied A_xM alloy and V_{avg} is the average voltage of a cell comprising an A_xM negative electrode

and a suitable cathode. To calculate the volumetric energy density of the A_xM alloys, a reference cathode needs to be chosen. For most of the metal-ion systems in this study, cathode materials have not been sufficiently investigated or are unknown entirely. For a valid comparison of anode materials, the same cathode voltage versus a standard reference electrode should be used. Keeping with the same convention as reference [9], cathode material with a voltage of 3.75 V versus Li metal was chosen in the calculations of energy density. This comparison may be not so unreasonable since in Li-ion battery chemistry, cathode voltage is limited by electrolyte stability, as the voltage stability of transition metal oxide based cathode materials can exceed that of the electrolyte [39] [40]. For other metal-ion systems, this same upper limit on cathode materials is likely to exist and, consequently, all high voltage cathode materials may have the same average voltage versus Li, as dictated by the stability of organic electrolyte solvents.

The average voltages of the A_xM alloys must also be known to calculate their energy density. Except for the case of Li alloys, the voltages of A_xM alloys have not been reported. To estimate the voltages of A_xM alloys, values of the formation energy of theoretical stable A_xM phases at 0 K were calculated by the "Materials Project" [41]. This web application uses density functional theory total energy calculations to compute the structure and 0 K formation energy of compounds [42]. The voltage of the A_xM alloy versus pure metal A, $V_A(A_xM)$, was then derived from the calculated free energy of formation, $E(A_xM)$, using the Nernst equation:

$$V_A(A_xM) = -\frac{E(A_xM)}{zxF} \quad (4)$$

Calculated voltage curves using this method were compared to the experimental potential profiles in the cases of Li-Si system (Figure 6), Li-Sn system (Figure 7), and Li-

Al system (Figure 8). The calculated average voltages curves have average voltages which are similar to the experimental results. Table 3 lists the calculated and experimental average voltages for Li_xM alloys. The calculated average potentials are close to the experimental values and vary by only tens of millivolts. From these comparisons, the predicted average potentials are quite acceptable in the scope of this study.

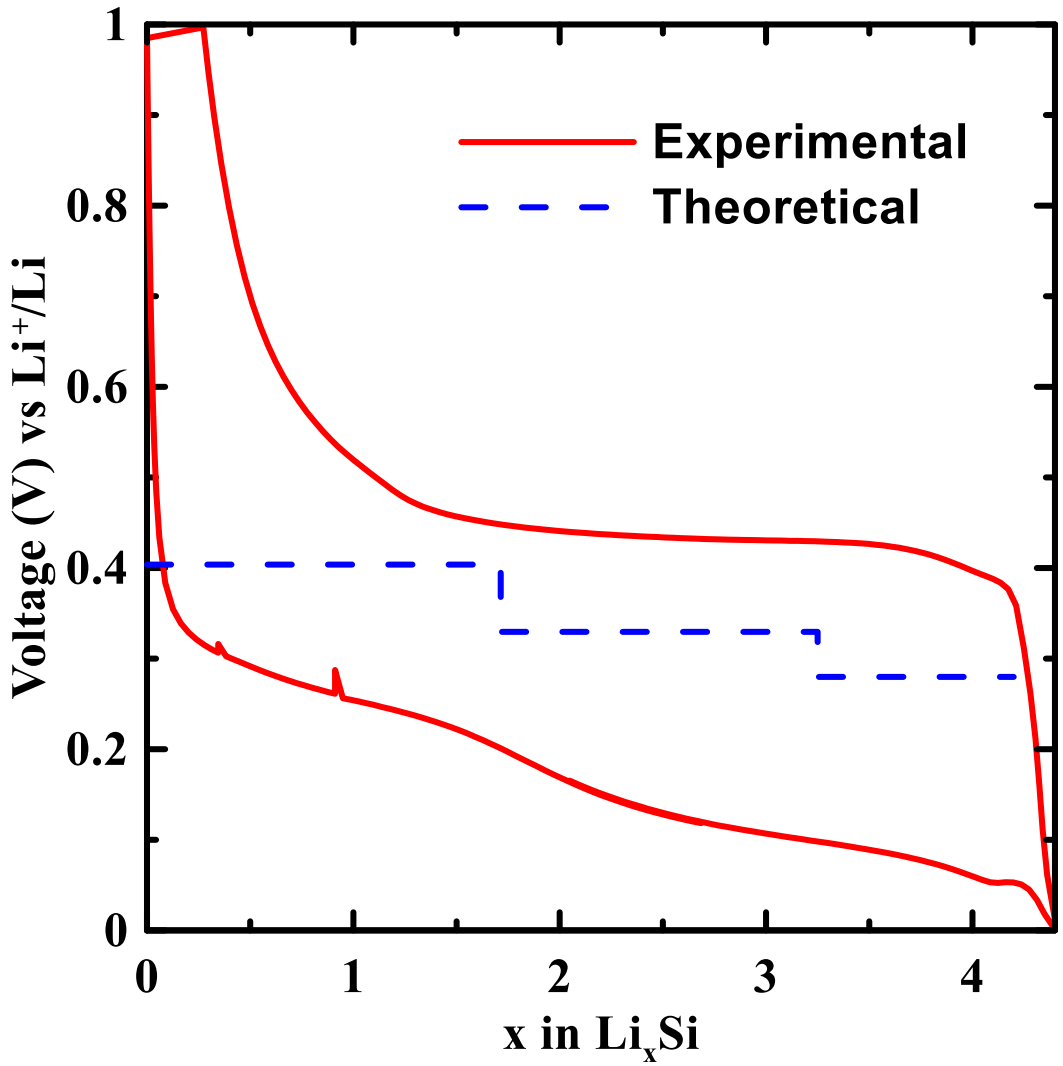

Figure 6 – The voltage curve of a silicon electrode cycled versus lithium metal.

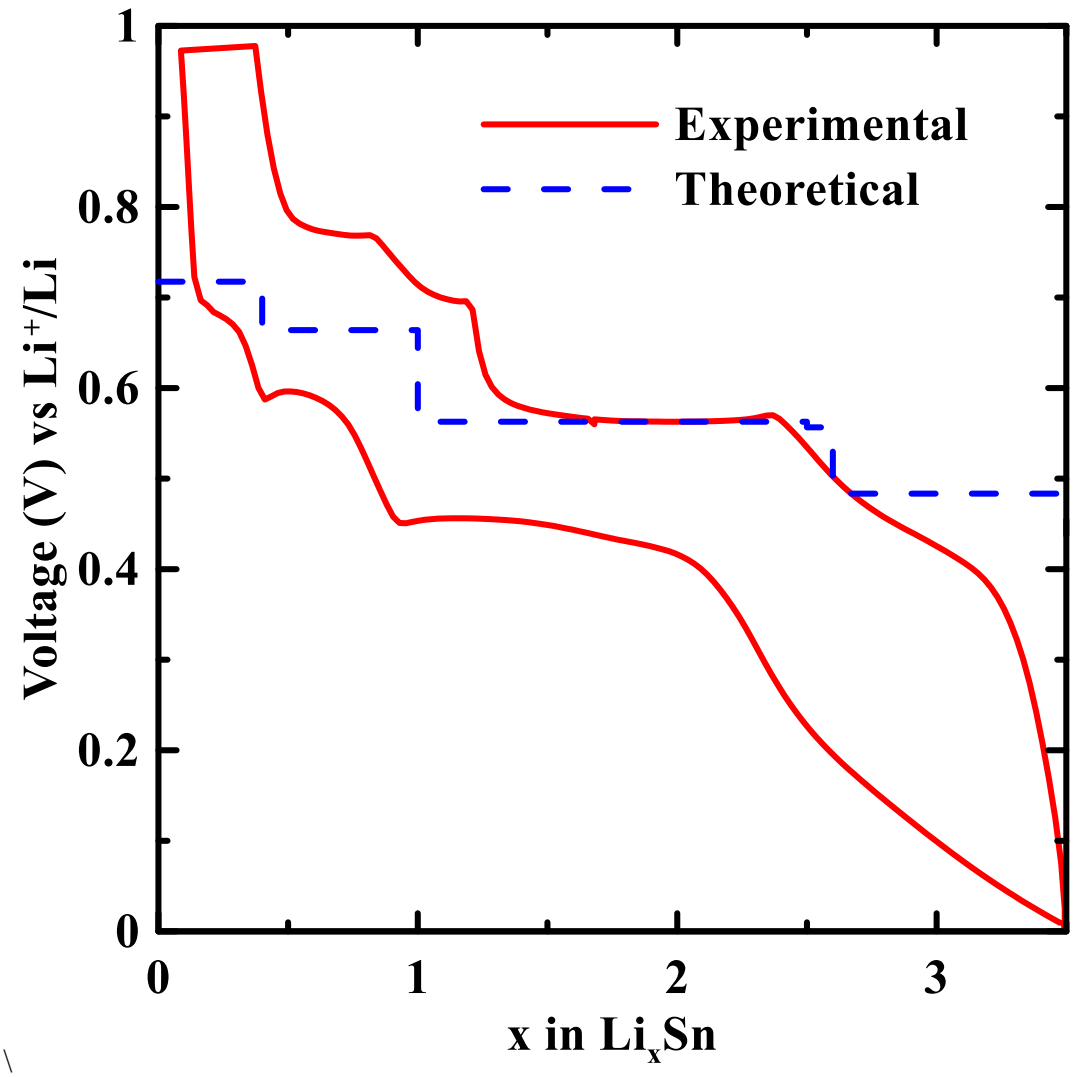

\

Figure 7 – The voltage curve of a tin electrode cycled versus lithium metal.

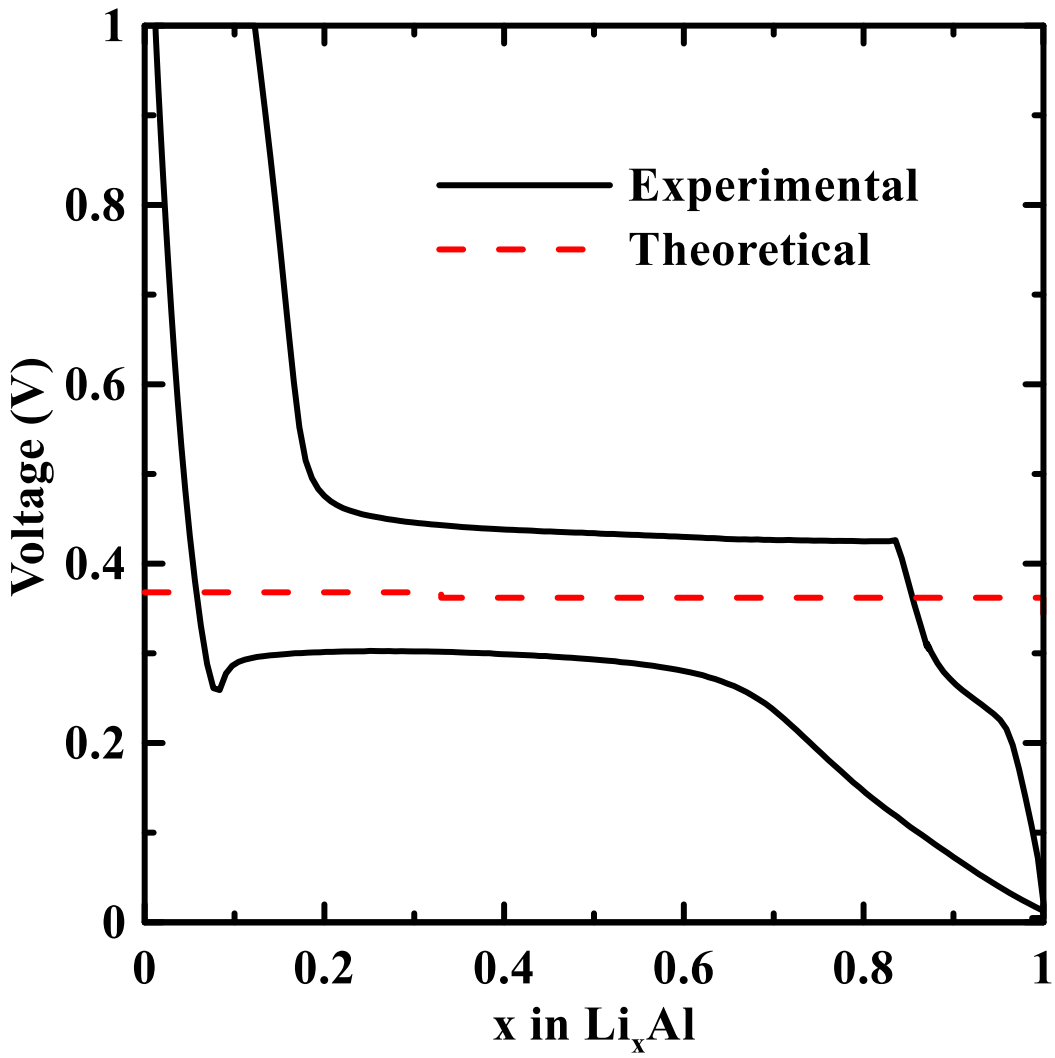

Figure 8 – The voltage curve of an aluminum electrode cycled versus lithium metal.

Table 3 – Observed average voltage (vs. Li) and the average voltage at 0K calculated from the Materials Project for some Li_xM alloys.

Alloy System	Average Voltage (V)	
	Calculated	Measured
Li_xSi	0.34	0.36
Li_xSn	0.57	0.51
Li_xAl	0.35	0.40

Using the same method, the average potentials for the rest of the alloys are summarized in Table 4. These potential can also be written with respect to lithium metal, which is a

more familiar reference potential. Using the standard reduction potentials of the guest metals, ε_A [43], the voltage of the A_xM alloy versus lithium metal, $V_{Li}(A_xM)$ is given by:

$$V_{Li}(A_xM) = V_A(A_xM) + (\varepsilon_A - \varepsilon_{Li}) \quad (5)$$

Table 4 – The volumetric capacity and average voltage at 0 K calculated from the Materials Project [41] for some A_xM alloys.
The voltage is calculated versus the pure metal A and also versus Li metal.

Fully Occupied A_xM Phase	Average Voltage (Volts vs. A)	Average Voltage (Volts vs. Li)	Volumetric Capacity (mAh/cc)
LiAl	0.35	0.35	1378
$Li_{15}Si_4$	0.34	0.34	2189
$Li_{4.4}Sn$	0.57	0.57	2024
$Na_{15}Sn_4$	0.37	0.70	1177
KSn	0.32	0.43	568
$Mg_{17}Al_{12}$	0.07	0.41	2582
Mg_2Si	0.25	0.59	2780
Mg_2Sn	0.57	0.91	2302
$CaAl_2$	1.00	1.17	1380
Ca_2Si	0.93	1.10	2150
Ca_2Sn	1.25	1.42	1851
Al_3Ti	0.83	2.21	6284
Al_6Mn	0.36	1.74	7355
$Al_{13}Fe_4$	0.72	2.10	7000
Al_2Cu	0.46	1.84	5950

The volumetric capacities shown in Table 4 have not accounted for the differences in volume expansion of different alloy systems. In order for alloy negative electrode materials to have practical application their volume expansion must be

managed. One method of doing this is by adding an inactive element in order to reduce the volume expansion of the alloy, so that it can be used in conventional composite electrode coatings. Such active/inactive alloys have higher volumetric energy density than if the volume expansion were limited simply cycling the pure A_xM alloy to a limited value of x [9]. The volume percent active component in an M/inactive alloy that results in a volume expansion of ξ_f at full state of charge is given by [9]:

$$\% \text{ volume active component in alloy} = \frac{\xi_f}{\xi_o} \times 100\% \quad (5)$$

where ξ_o is the percent expansion of the pure alloy A_xM at full state of charge ($x = x_f$).

Table 5 lists the volume percent active component in M/inactive alloys that expand by 100% at full state of charge and their corresponding volumetric energy densities. Using a 3.75 V versus Li metal reference cathode and the calculated average alloy voltage, as described in Table 4, the volumetric energy density of A_xM alloys were calculated using equation (3). The typical energy density of a conventional graphitic negative electrode in a lithium ion cell (LiC_6, 350 mAh/g, 150 mV vs. Li) is also shown for comparison. These energy densities represent what one might expect to achieve in practical A-ion cells using alloy anodes.

Table 5 – The volumetric energy density of some A_xM alloys versus a 3.75 V (vs. Li) cathode. Also listed is the percent by volume of the metal M required in a M/inactive alloy that expands by 100% at full state of charge and the energy density of such an alloy. The volumetric energy density of a conventional graphite negative electrode material for lithium ion batteries is listed for comparison.

Fully Occupied A_xM Phase	Volumetric Energy Density (Wh/L)	% Active to Obtain 100% Expansion Alloy	Energy Density of 100% Expansion Alloy (Wh/L)
LiC_6	2591	-	-
LiAl	4689	-	-
$Li_{15}Si_4$	7468	36	5064
$Li_{4.4}Sn$	6437	39	4468
$Na_{15}Sn_4$	3590	24	2218
KSn	1889	53	1443
$Mg_{17}Al_{12}$	8636	51	6541
Mg_2Si	8797	45	6399
Mg_2Sn	6531	54	5022
$CaAl_2$	3560	-	-
Ca_2Si	5690	32	3752
Ca_2Sn	4317	39	3003
Al_3Ti	9690	13	5477
Al_6Mn	14805	38	10237
Al_2Cu	11376	23	7022
$Al_{13}Fe_4$	11583	36	7860

2.4 Conclusions

In this chapter, the volume expansion behavior and volumetric energy densities of metal alloy negative electrodes (A_xM) for metal-ion batteries based on A = Li, Na, K, Mg, Ca and Al were compared. Based on known alloy phases, all of the alloys are

expected to have linear volume expansion with state of charge. Furthermore it was found that each metal ion, A, has a characteristic volume in alloys which is almost insensitive to the host metal, M. All alloy systems, with the exception of K_xM alloys, were found to have similar or greater volumetric energy density than conventional graphitic anodes in Li-ion cells. It is predicted that both the Mg_xM and Al_xM systems might achieve higher energy densities than possible with any Li-ion negative electrode known. The Al_xM system is particularly interesting, since energy densities of up to four times the energy density of graphite electrodes used in a lithium ion cell might be achieved in M/inactive alloys that expand by only 100% using inexpensive transition metals and at an average voltage of about 2 V. It is still not known if Al can be incorporated in alloys electrochemically. In contrast, magnesium has been recently observed to be able to insert into Sn and Sb reversibly [18]. Additionally, reversible electrochemical alloying of Mg in Pb will be described below. If such alloys can be developed for use in practical cells, much higher energy density batteries than conventional Li-ion cells might be achieved.

CHAPTER 3
ELECTROLYTE STUDY FOR MAGNESIUM-BASED BATTERIES [‡]

3.1 Introduction

As stated in Chapter 1, the three main parts of an electrochemical cell are the positive electrode, the negative electrode and the electrolyte. Amongst these, the electrolyte which allows metal ions to travel between the positive electrode and the negative electrode, plays a very important role. However, one of the biggest challenges for the development of practical Mg-based batteries is the development of a practical electrolyte. While Li-ion batteries use electrolytes containing lithium hexafluorophosphate ($LiPF_6$) salt, dissolved in organic carbonate-based solvents, such as mixtures of EC, DEC or propylene carbonate (PC), practical analogues of these electrolytes for Mg-based batteries have not been demonstrated. Mg salts (perchlorate, chloride, triflate) have low solubility in such solvents [44]. Additionally, using such salts Lu reported that alkyl carbonates and acetonitrile solvents form a thick passivation layer on Mg metal, making Mg deposition impossible [44].

Mo_6S_8 is so called Chevrel phase material which was reported in 1971 [10]. The building block of this material contains 8 S atoms forming a rhombohedral cube (space

[‡] Materials from this chapter were used with permission from T.T. Tran, W.M. Lamanna, and M.N. Obrovac, *J. Electrochem. Soc.*, **159** (2012) A2005. T.T. Tran's contribution to this publication was: developing synthetic technique of Mo_6S_8, designing 3-electrode coin cell, performing electrochemical experiments, and co-authoring the manuscript text. $Mg(TFSI)_2$ salt was synthesized and analyzed by W.M. Lamanna at 3M.

group R-3) which contains a Mo_6 octahedron inside [45]. The detail of lattice parameters for Mo_6S_8 structure is well defined in reference [46].

Recent work, especially from the Aurbach group, has resulted in the development of Grignard-based electrolytes with sufficiently high oxidation potentials to demonstrate reversible Mo_6S_8 vs. Mg batteries [47-49]. Typically, Grignard-based electrolytes are composed of a solution of magnesium alkyl halide in tetrahydrofuran (THF). The practicality of such electrolytes is questionable, since they are flammable, toxic, unstable and reactive in air. They are also corrosive towards cell hardware [50].

Recently, reversible cycling of a Bi vs. Mg cell has been reported in an electrolyte composed of $Mg(TFSI)_2$ in acetonitrile [18]. Such an electrolyte system is attractive since, $Mg(TFSI)_2$ has a high solubility in organic solvents and acetonitrile is highly oxidatively stable. However, the operation of this electrolyte at low voltages is surprising since, previous reports claim that acetonitrile-based electrolytes, form a passivating layer on Mg at low voltages, creating prohibitively high overpotentials for Mg plating [44]. Furthermore, acetonitrile is known to be reductively unstable and electrolytes containing TFSI salts are known to be corrosive towards aluminum cell parts when used in lithium ion cells [19]. These could lead to potential issues for the use of this electrolyte in practical Mg cells. Therefore in this chapter, a detailed study of the use of $Mg(TFSI)_2$/AN electrolyte for Mg-based batteries will be conducted.

3.2 Experimental

Because of the reversibility magnesiate and de-magnesiate of Mo_6S_8, Mo_6S_8 vs. Mg cells were chosen as a reference to evaluate the performance of different electrolyte

systems. Additional cells using stainless steel working electrodes were used to determine the potential window of electrolytes.

Mo_6S_8 is a thermodynamically unstable material that cannot be directly synthesized [51]. It is typically made by leaching copper from $Cu_2Mo_6S_8$ [51]. $Cu_2Mo_6S_8$ was synthesized according to the method of reference [52]: a stoichiometric mixture of Cu powder (Alfa Aesar, -325 mesh, 99%), Mo powder (Sigma Aldrich, 1-2 μm, >99.9%) and MoS_2 powder (Alfa Aesar, -325 mesh, 99%) were heated to 985°C under vacuum to form $Cu_2Mo_6S_8$. Cu was then leached from $Cu_2Mo_6S_8$ according to the method described in reference [51]: the $Cu_2Mo_6S_8$ powder was placed in an excess of 6 M HCl while stirring under bubbling O_2 for at least 12 hours. After leaching, the Mo_6S_8 product was collected by centrifuging, then washed with distilled water and air dried at 150°C for 2 hours.

Mo_6S_8 electrodes were prepared by making a slurry containing 80/10/10 of Mo_6S_8, carbon black (Super-P, Timcal, Switzerland) and polyvinylidene difluoride (PVDF) (Kynar HSV-900) by weight. An additional 5 grams of N-methylpyrrolidone (NMP) (Sigma Aldrich, 99.5%) for every 2 grams of mixture were added in order to achieve a proper consistency for coating. The slurry was then mixed for 2 hours at 200 rpm using planetary mill with two 3/8" tungsten carbide balls and then coated onto aluminum foil using a coating bar with a 0.006 inch gap, followed by air drying at 120°C for 2 hours. The electrodes for electrochemical study in coin cells were cut from this coating using a 2 cm diameter circular punch. The weight of an electrode was determined using an AND GR-202 analytical balance (±1 mg resolution).

$Mg(TFSI)_2$ was prepared by William Lammana at 3M company by the neutralization of a 55.5 wt% solution $H\text{-}N(SO_2CF_3)_2$ in water with magnesium metal. The water was evaporated from the resulting solution and the residual $Mg(TFSI)_2$ was vacuum dried overnight at 145°C. Analysis of the product by quantitative ^1H and ^{19}F NMR spectroscopy indicated that it was of high purity, containing > 99.9% by wt. $Mg(TFSI)_2$. Water levels measured by Karl-Fischer analysis were 34 ppm and tetrahydrofuran ion levels measured by chromatography were < 3 ppm. Levels of common metal ion impurities (24 element scan) were determined by ICP-MS and all metallic impurities were found to be present at less than 3 ppm in the product.

Acetonitrile-based electrolytes were prepared in an Ar-filled glovebox by dissolving an appropriate amount of $Mg(TFSI)_2$ in acetonitrile (Sigma Aldrich, 99.9%) which was pre-dried with molecular sieves (Sigma Aldrich, 3Å beads, 4-8 mesh).

A Grignard-based all-ethyl-complex (AEC) in THF electrolyte was made by drop-wise adding a 0.5 M aluminum chloride ($AlCl_3$) in THF solution into a 2 M ethyl magnesium chloride (EtMgCl) in THF solution (both solutions used as received from Aldrich) in 1:2 mole ratio. An appropriate amount of THF (Sigma Aldrich, anhydrous, 99.9%) was added to obtain 0.25 M of EtMgCl in THF solution.

2-electrode and 3-electrode coin cells were prepared in this study. In electrochemistry, experiments using a 3-electrode system are usually conducted in flooded beaker-type or flask cells. These type of cells generally need large quantities of electrolyte (compared to the ~100 µL used in a coin cell) and do not provide stack pressure to maintain the structural integrity of electrodes which may change volume during cycling. 3-electrode coin cells are one alternative construction that may be

developed in order to gather voltage information at the positive and the negative electrodes while maintaining internal pressure of the cell and using minimal electrolyte volumes. In this cell, a magnesium strip reference electrode was placed between the positive electrode and the negative electrode. The role of this reference electrode is to provide a constant reference potential against both the working electrode and counter electrode which are measured while cycling the cell.

2-electrode and 3-electrode coin cells construction is shown schematically in Figure 9. The 2-electrode cell stack consists of a conical spring, spacer, working electrode, 2 layers of Celgard® 2301 separator, and a counter/reference electrode. All electrodes and separators were made wet with electrolyte as they were placed in the cell. 3-electrode coin cells were made similarly, except a Mg wire reference electrode was placed in the center of the cell stack, between the two polypropylene blown microfiber separators (BMF, ~190 μm thick, 3M Company) which were placed between 2 Celgard® 2301 separators. The wire exited the cell through a hole in the cell can, which was sealed with Torr Seal epoxy resin (Varian) after the cell was crimped.

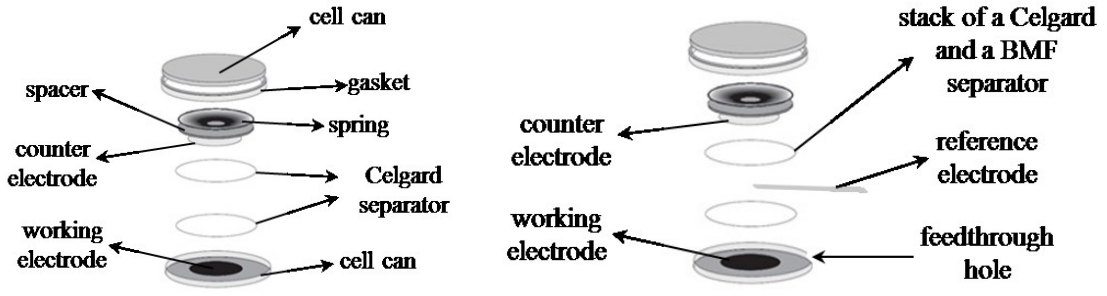

(a) (b)

Figure 9 – Schematic drawing of the (a) 2-electrode coin cells and (b) 3-electrode coin cells used in this study.

2-electrode and 3-electrode cells are identified here according to their construction as: working/counter and working/reference/counter, respectively. Electrolytes are identified as salt/solvent. Electrochemical testing of 2-electrode cells was performed using a Maccor Series 4000 Automated Test System. Electrochemical testing of 3-electrode cells was performed using a Biologic SP-300 potentiostat/galvanostat.

X-ray diffraction (XRD) measurements were performed with a Siemens D5000 diffractometer using a Cu target and a diffracted beam monochromator. Cells used for XRD measurements were disassembled in an argon-filled glovebox after cycling. The cycled electrode material was then rinsed with the same solvent as used in the cell electrolyte (acetonitrile or THF), dried under vacuum, and placed on a zero-background Si wafer in a gas-tight sample holder (described in reference [53]) for powder XRD studies.

3.3 Results

In order to determine the electrochemical window of $Mg(TFSI)_2$/AN electrolyte and its efficacy for Mg plating, cyclic voltammetry (CV) measurements using 3-electrode cells with a Mg reference and Mg counter electrode were first attempted. During CV measurements very large reducing potentials (< -5 V vs. Mg) were encountered at the counter electrode, which were outside the operational range of the potentiostat. Without a reasonably non-polarizable counter electrode available, such measurements were not useful. Instead, galvanostatic measurements were made at small currents to avoid large overpotentials at the Mg counter electrode. The current used (0.01 mAh/cm^2) was about

equal to the current used in Mo_6S_8 cells discussed below, which were cycled at a C/100 rate.

Figure 10 shows the voltage behaviour of a Mg working electrode in a Mg/Mg/Mg 3-electrode cell with a 0.5 M $Mg(TFSI)_2$ /AN electrolyte. In the Figure 10, Mg appears to be reversibly stripping and plating on the working electrode. However, while the overpotential for stripping Mg becomes relatively stable with cycling, the overpotential for plating is not stable. It is likely that a different mechanism than Mg plating is occurring at low potentials, causing this unstable behaviour.

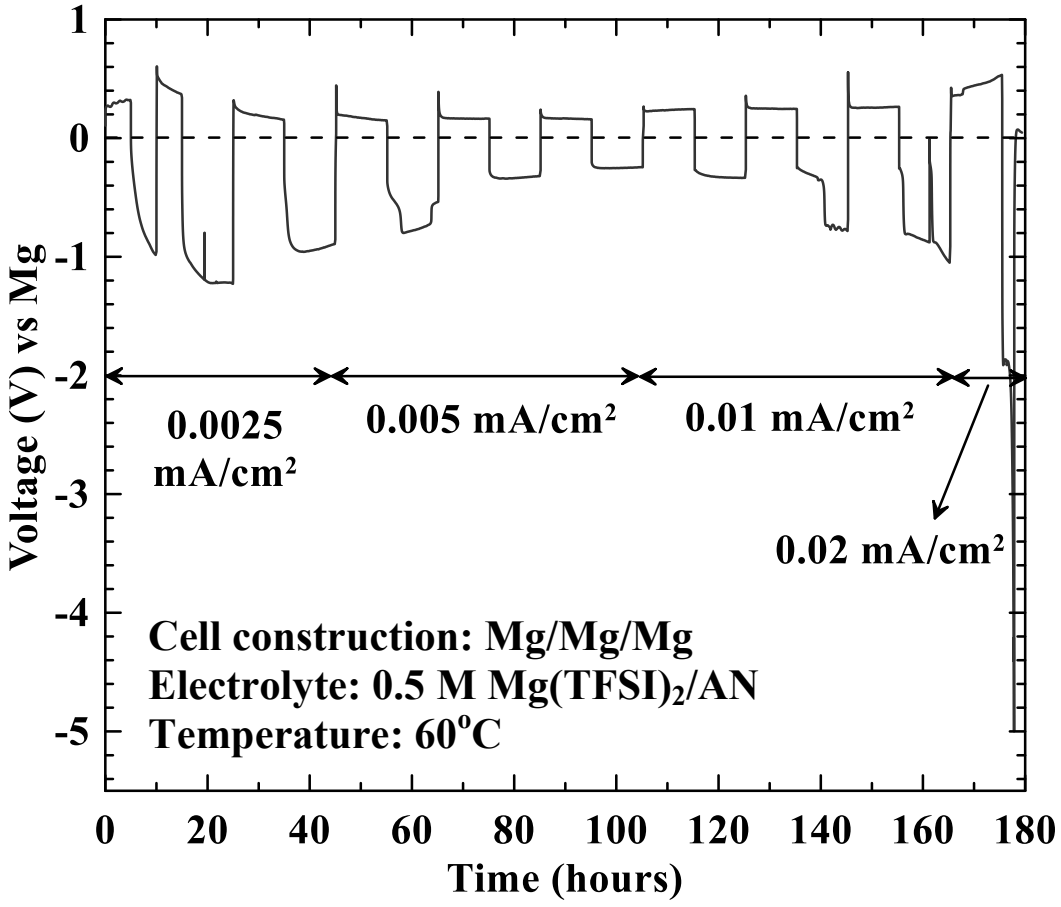

Figure 10 – Anodic and cathodic galvanostatic behaviour of a magnesium electrode in $Mg(TFSI)_2$/AN electrolyte.

Figure 11 shows the voltage curves of a 3-electrode cell with a stainless steel (SS) working electrode, Mg reference electrode and Mg counter electrode. During the first half-cycle Mg plating was attempted on the SS electrode, while Mg was stripped from the Mg counter electrode. The stripping of Mg occurs at about 0.5V vs. Mg on the counter electrode, while a reduction reaction at the SS electrode occurs at about -1.3 V vs. Mg. After this step, the cell was allowed to rest at open circuit for 60 hours. As expected, the voltage of the Mg counter electrode quickly approached zero volts versus the Mg reference electrode during the rest step. However, the SS electrode voltage equilibrated at about 1 V vs. Mg. This result indicates that no Mg has been plated on the SS surface. It is likely then, that $Mg(TFSI)_2$/AN reduction is occurring rather than Mg plating on the SS electrode.

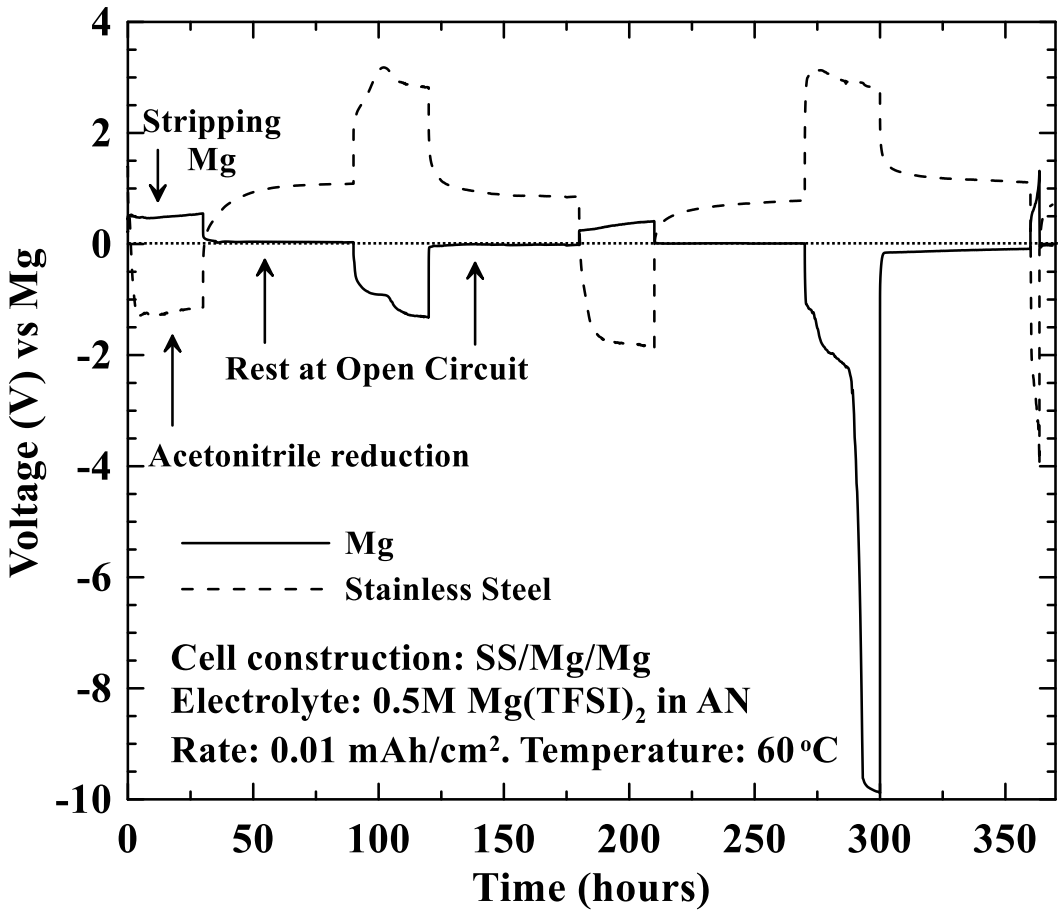

Figure 11 – Voltage profile of a SS/Mg/Mg cell with 0.5M $Mg(TFSI)_2$/AN electrolyte operating at 60°C. The cell was started in the direction corresponding to reduction at the stainless steel working electrode.

According to Figure 10, the $Mg(TFSI)_2$/AN reduction can occur at voltages as low as -0.2 V vs. Mg. This indicates that the minimum voltage at which $Mg(TFSI)_2$/AN reduction takes place can be less negative than -0.2 V vs. Mg. It is interesting that this voltage is more negative than the plating potential of Mg, yet no plating takes place. As a result, a large overpotential for Mg plating exists in this electrolyte system, likely because a passivating SEI layer is formed that does not conduct Mg^{2+} ions. High plating overpotentials due to ionically insulating SEI layers have also been observed during attempted plating of Mg from other conventional electrolytes [44]. Result from stripping

Mg in other conventional electrolytes also shows that at high positive potentials such passivating surface films break down, enabling Mg dissolution [44]. Evidently the voltage at which the passivating surface film breaks down in $Mg(TFSI)_2$/AN is low, leading to a low overpotential for Mg stripping. This is consistent with the corrosive nature of electrolytes containing TFSI salts [19].

Further cycling of the cell of Figure 11 resulted in large reducing overpotentials on the SS electrode, presumably caused by electrolyte depletion or gas formation. This is likely the cause of the large reducing potentials observed during CV studies and the instability in reduction overpotentials observed in Figure 10.

Figure 12 shows the voltage curves of the working and counter electrodes in an identical cell to the one used in Figure 11, but started in the direction corresponding to oxidation of the SS working electrode and reduction at the Mg counter electrode. The SS electrode has an oxidation plateau at about 2.8 V vs. Mg during this process. Since acetonitrile is expected to be oxidatively stable, this plateau is likely due to the corrosion of SS in this electrolyte. This corrosion potential is slightly higher than reported for the corrosion of stainless steel in Grignard-based electrolytes, which is about 2.5 V [50]. It should be emphasized that a stainless steel working electrode was used here, since stainless steel is commonly used for commercial cell hardware. Higher voltages are likely to be obtained before the onset of corrosion reactions if other working electrodes, such as platinum or glassy carbon, are used.

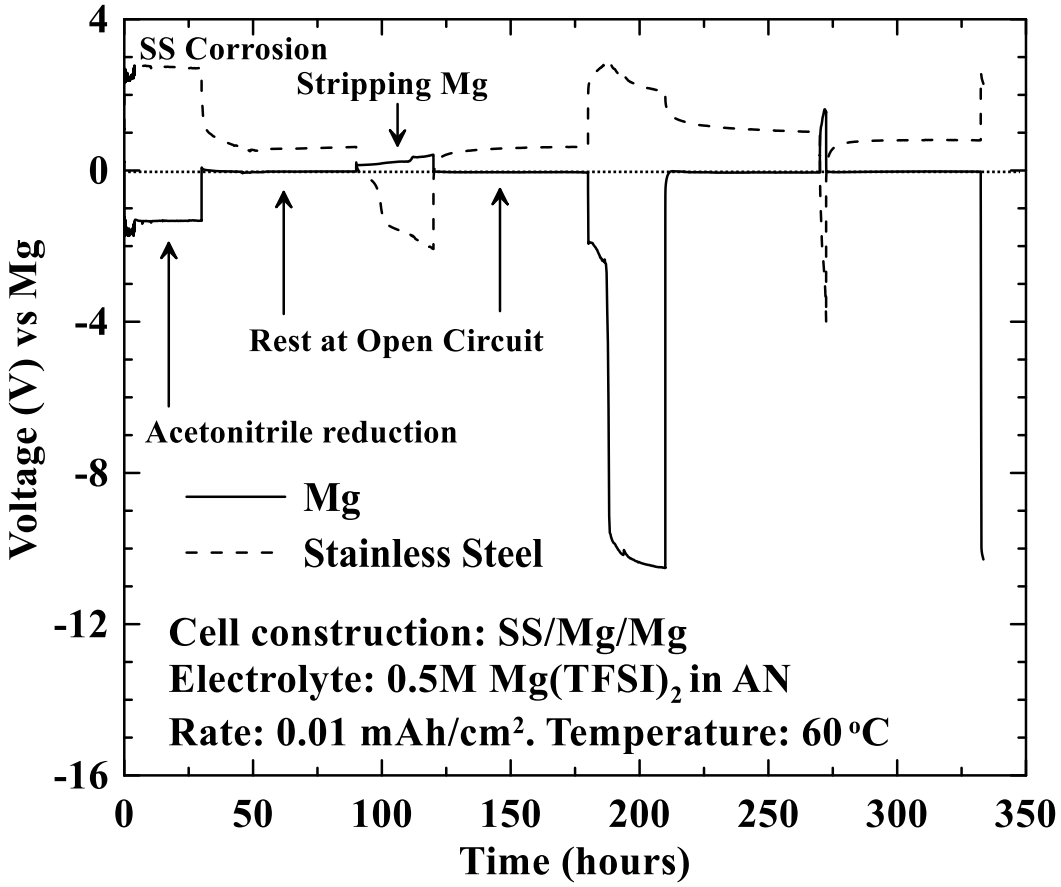

Figure 12 – Voltage profile of a SS/Mg/Mg cell with 0.5M $Mg(TFSI)_2$/AN electrolyte operating at 60°C. The cell was started in the direction corresponding to oxidation at the stainless steel working electrode.

In order to evaluate $Mg(TFSI)_2$/AN electrolyte in working magnesium cells, Mo_6S_8 electrodes were prepared. Figure 13 shows the XRD pattern of copper containing Chevrel phase made by direct reaction of Cu, MoS_2 and Mo at 985°C. The pattern shows that this method of producing the copper Chevrel phase resulted in a 2-phase mixture of $Cu_2Mo_6S_8$ with some $Cu_{0.9}Mo_3S_4$. Figure 14 shows the XRD pattern of the $Cu_2Mo_6S_8$/ $Cu_{0.9}Mo_6S_8$ sample after leaching, which is phase pure Mo_6S_8. Apparently both copper containing phases form Mo_6S_8 Chevrel phase upon leaching.

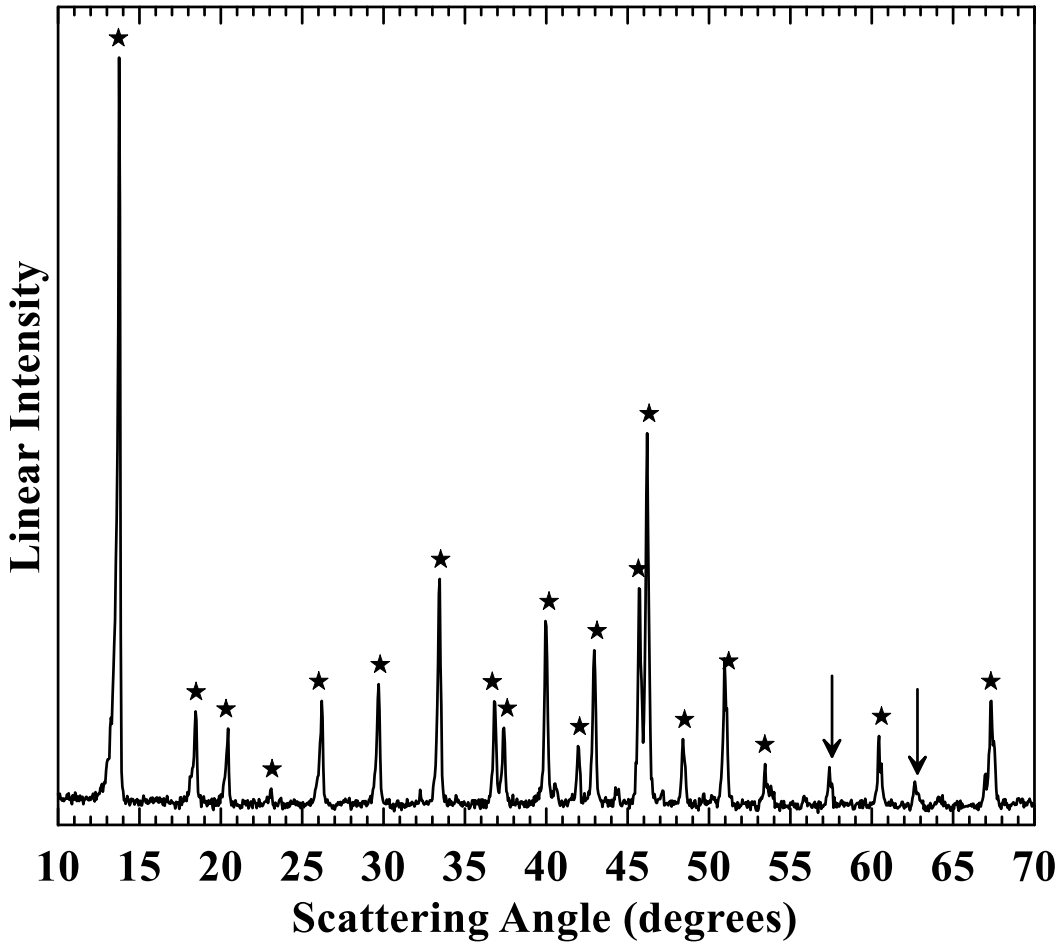

Figure 13 – XRD pattern of $Cu_2Mo_6S_8$. The stars and arrows indicate peak positions from $Cu_2Mo_6S_8$ (PDF 00-047-1519) and $Cu_{0.9}Mo_3S_4$ (PDF 00-071-0215), respectively [25].

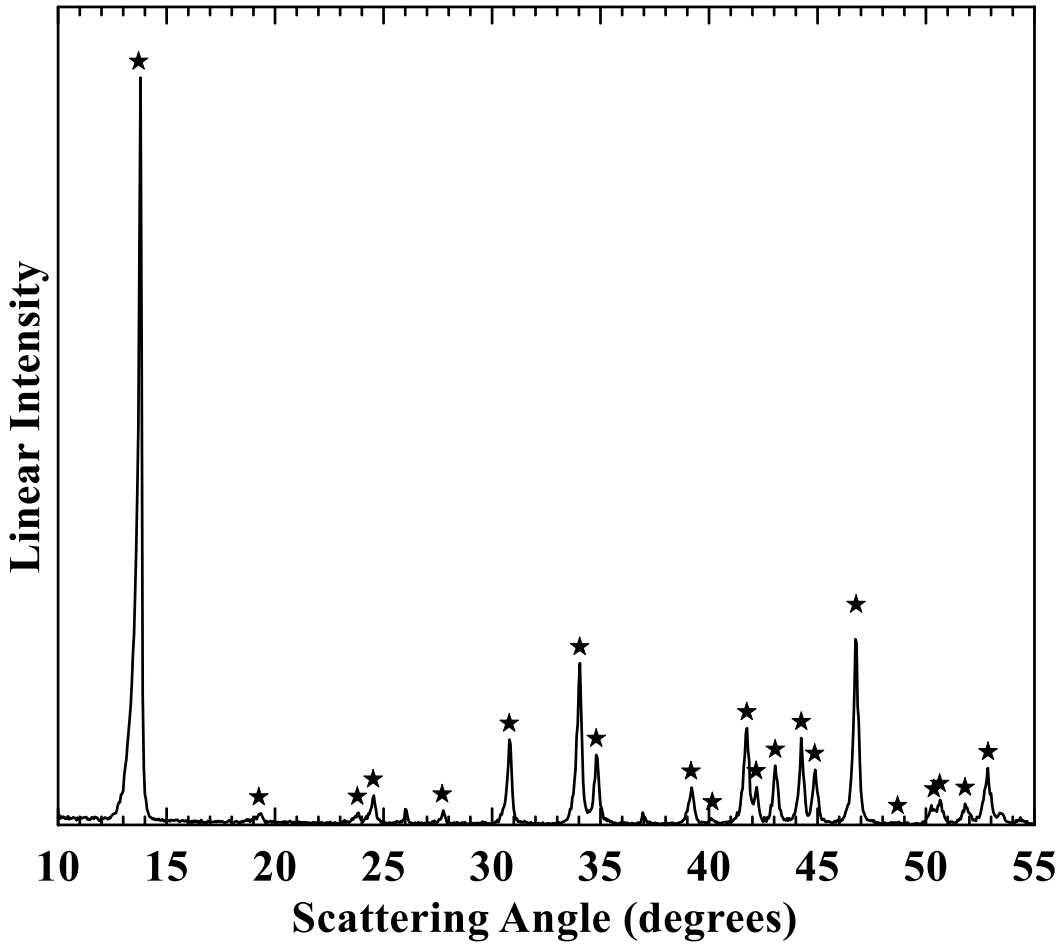

Figure 14 – XRD of Mo_6S_8. The stars indicate peak positions from Mo_6S_8 (PDF 00-027-0319) [25].

Mo_6S_8 vs. Mg coin cells using AEC/THF electrolyte were made to verify the performance of Mo_6S_8 electrodes in a Grignard-based electrolyte. Figure 15a shows the first 1.5 cycles of this cell at 30°C. The first discharge consists of a single plateau of about 130 mAh/g, corresponding to the insertion of 2 formula units of Mg. Only one Mg can be inserted and removed during the subsequent cycle along a single plateau with an average voltage of about 1.1 V. The irreversible capacity is quite high. This behaviour is consistent with that reported earlier for Mo_6S_8 derived from HCl leaching [51], although polarization and irreversible capacity is greater in the cells from this study (59%

irreversible capacity in the cells in this study compared to 38% irreversible capacity from reference [51]). This is likely because the sizes of Mo_6S_8 particles synthesized above are larger, as a consequence of the method of precursor synthesis in this study. Figure 15b shows one cycle of the same cell, now cycled at 60°C. At this temperature additional magnesium can be reversibly intercalated into Mo_6S_8, along second plateau having an average voltage of about 1.45V. This plateau has higher polarization than the low voltage plateau and only can be accessed at elevated temperatures. This also agrees well with previous studies [51].

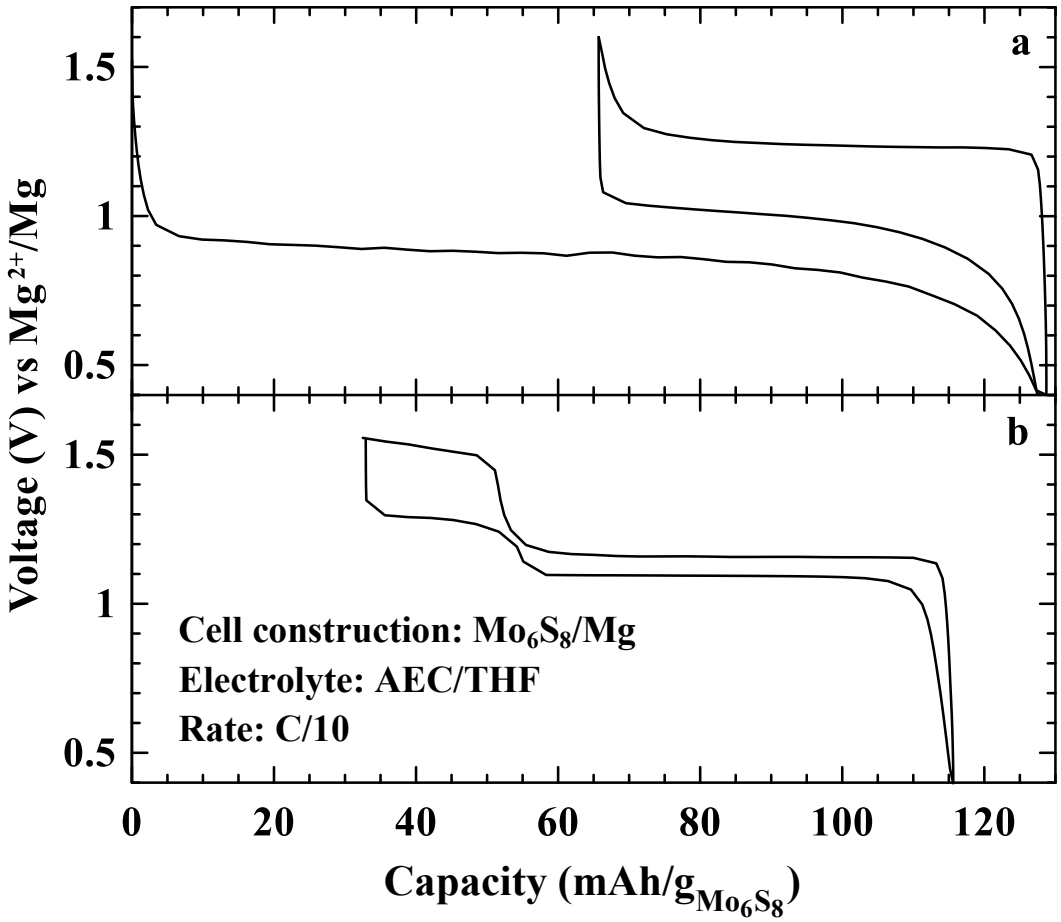

Figure 15 – Voltage curve of a Mo_6S_8/Mg coin cell with AEC/THF electrolyte. (a) First 1.5 cycles at 30°C and (b) subsequent cycle at 60°C.

Figure 16 shows the magnesiating process of Mo_6S_8 versus Mg cells operated at 30°C and 60°C with 0.5 M $Mg(TFSI)_2$/AN electrolyte. At 30°C about 40% of the theoretical capacity of Mo_6S_8 is achieved, while about 98% of the theoretical capacity was obtained at 60°C. This is similar to the behaviour observed in AEC/THF electrolyte. Although polarization was high in these cells, it likely originates from the Mg counter/reference electrode. Results from 3-electrode measurements are discussed below.

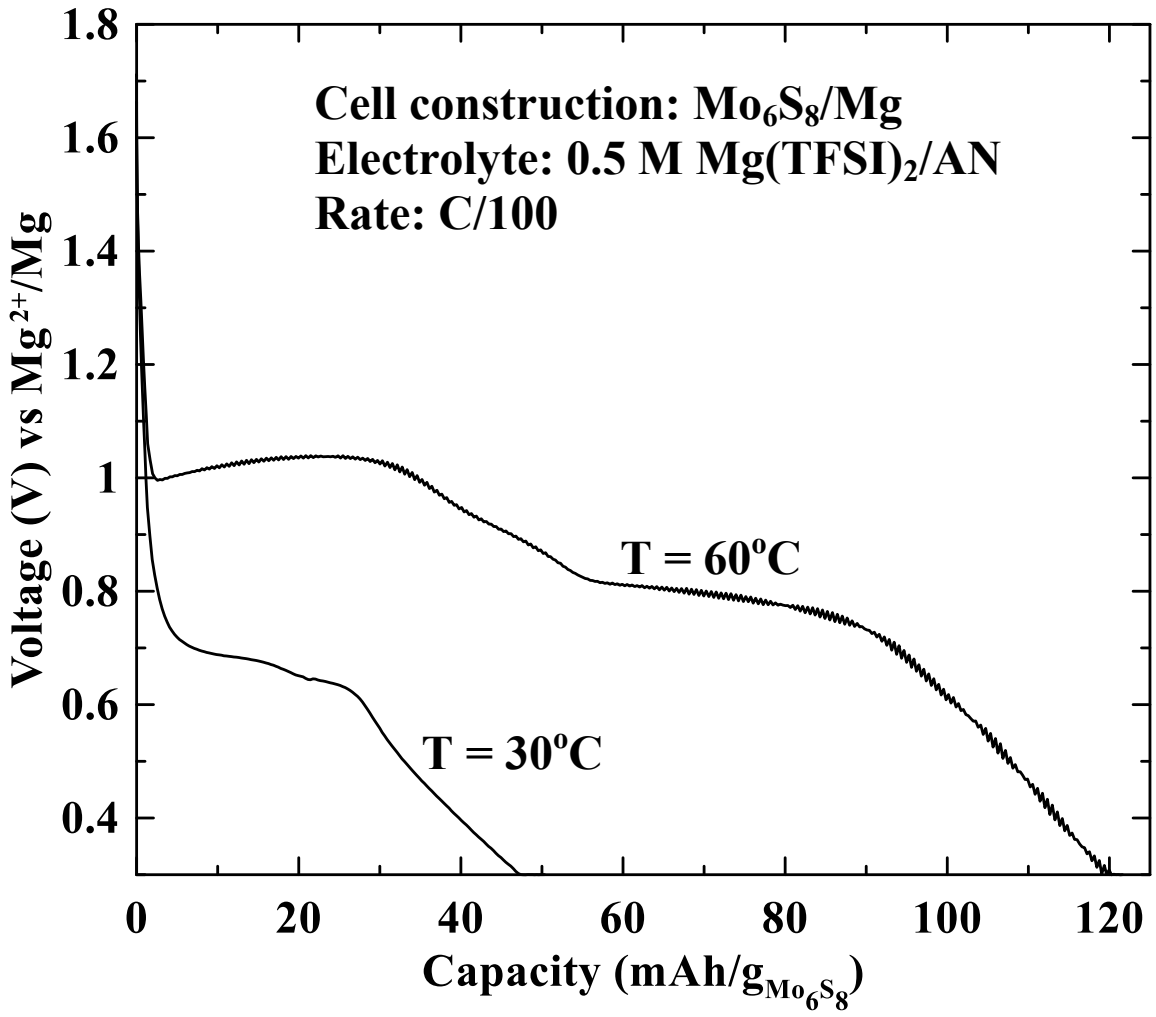

Figure 16 – Voltage profile of the first discharge of Mo_6S_8/Mg cells with 0.5M $Mg(TFSI)_2$/AN electrolyte operated at 30°C and 60°C.

To confirm the magnesiation of Mo_6S_8 is occurring in these cells, Mo_6S_8/Mg cell with $Mg(TFSI)_2$/AN electrolyte fully discharged at 60°C was disassembled in a He-filled glovebox for ex-situ XRD study of the working electrode. Figure 17 shows the resulting XRD pattern, which consists primarily of fully magnesiated $Mg_2Mo_6S_8$ with a small amount of $MgMo_6S_8$, confirming that magnesiation of Mo_6S_8 has occurred in the cell. Peaks in the XRD pattern at 20, 26, 21.5, 53 and 57° could not be identified. These may be from residual salt in the electrode or possibly reaction of the electrode with air due to imperfect sealing of the sample holder.

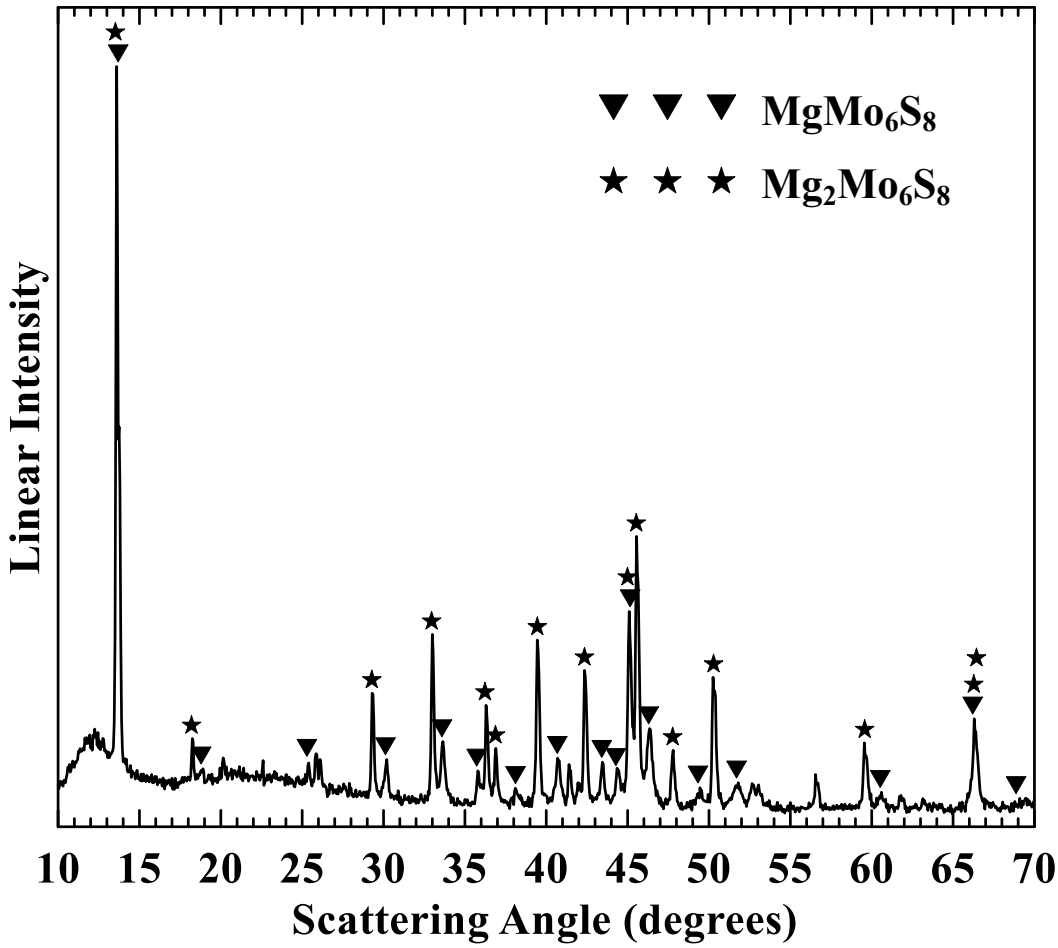

Figure 17 – XRD measurement of a Mo_6S_8 electrode after undergoing magnesiation at 60°C in a Mo_6S_8/Mg cell with 0.5M $Mg(TFSI)_2$/AN electrolyte. Peak positions from $MgMo_6S_8$ and $Mg_2Mo_6S_8$ are indicated according to reference [51].

Using the magnesiated Mo_6S_8 electrode harvested from the above Mg/Mo_6S_8 cell, a symmetric cell containing this electrode and a fresh Mo_6S_8 electrode was made. This cell was cycled over the high voltage plateau with 0.5 M $Mg(TFSI)_2$/AN electrolyte. Figure 18 shows the voltage curve of this cell, which is highly reversible and clearly demonstrates that Mo_6S_8 electrodes can be reversibly cycled in acetonitrile-based electrolyte.

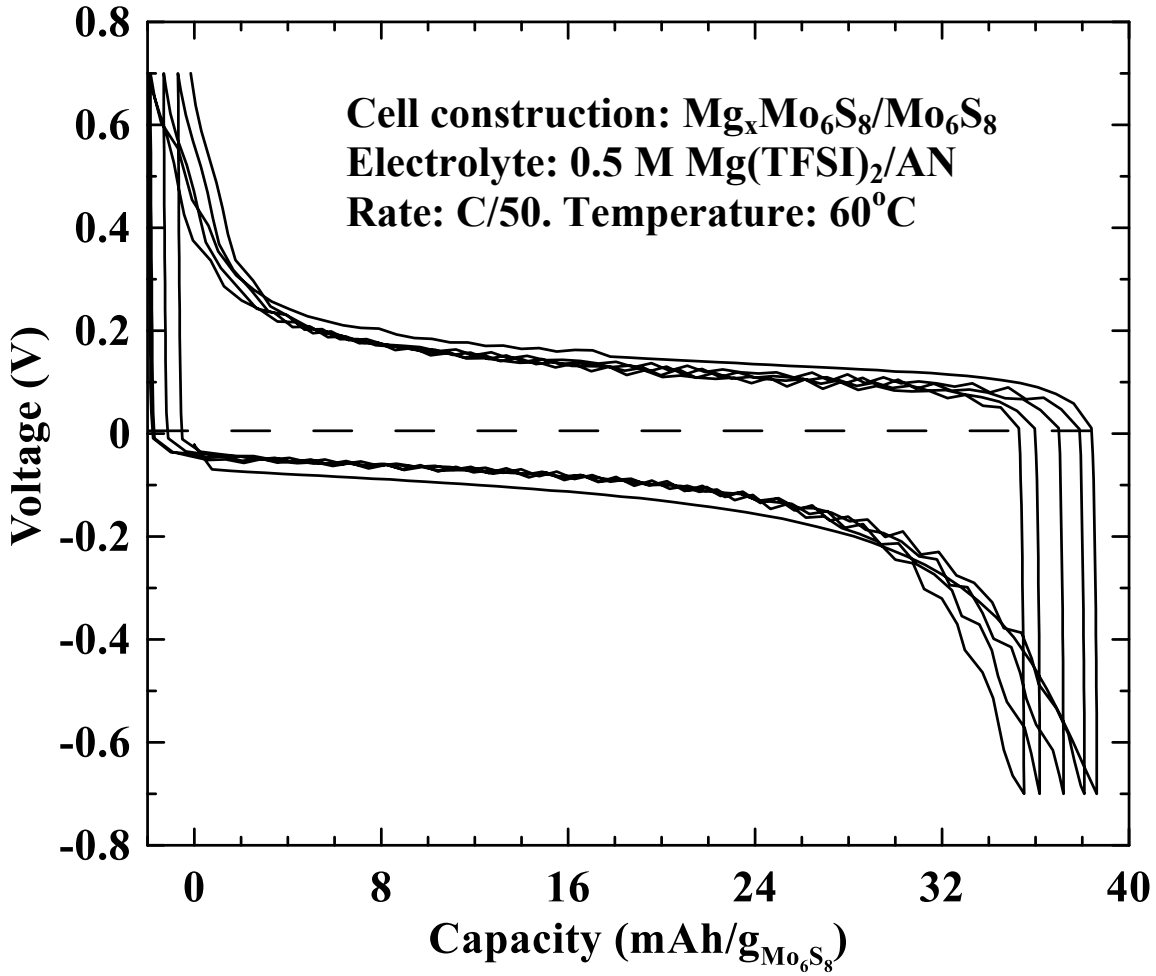

Figure 18 – Voltage profile a $Mg_xMo_6S_8/Mo_6S_8$ symmetric cell with 0.5M $Mg(TFSI)_2$/AN electrolyte.

3-electrode cells consisting of a Mo_6S_8 working electrode, Mg counter electrode and Mg reference electrode were constructed to accurately measure the voltage behavior of the Mo_6S_8 electrode in $Mg(TFSI)_2$/AN electrolyte. Figure 19 shows the voltage profile of the Mo_6S_8 working electrode at 60°C during the first two cycles. The voltage curve is similar to that of Mo_6S_8 in AEC/THF electrolyte, shown in Figure 15, excepting that the capacity obtained in $Mg(TFSI)_2$/AN electrolyte is significantly higher, reaching nearly the theoretical capacity of Mo_6S_8. The irreversible capacity is also very low (5%), compared to cells cycled in THF-based electrolyte (~38% in reference [51]). This is a significant advantage for this electrolyte towards practical cells. However the average voltage of the two plateaus is about 0.2 V lower in $Mg(TFSI)_2$/AN (0.9 V, 1.1 V), compared to that observed in AEC/THF (1.1 V, 1.45 V). This behavior is not understood. Since both plateaus are equally effected, it is possible that a shift in the Mg reference electrode voltage occurs in $Mg(TFSI)_2$/AN electrolyte compared to Mg in AEC/THF electrolyte. This might happen, for instance, if the decomposition products of acetonitrile reduction form a conductive layer on the Mg reference electrode. This is pure speculation and requires further study.

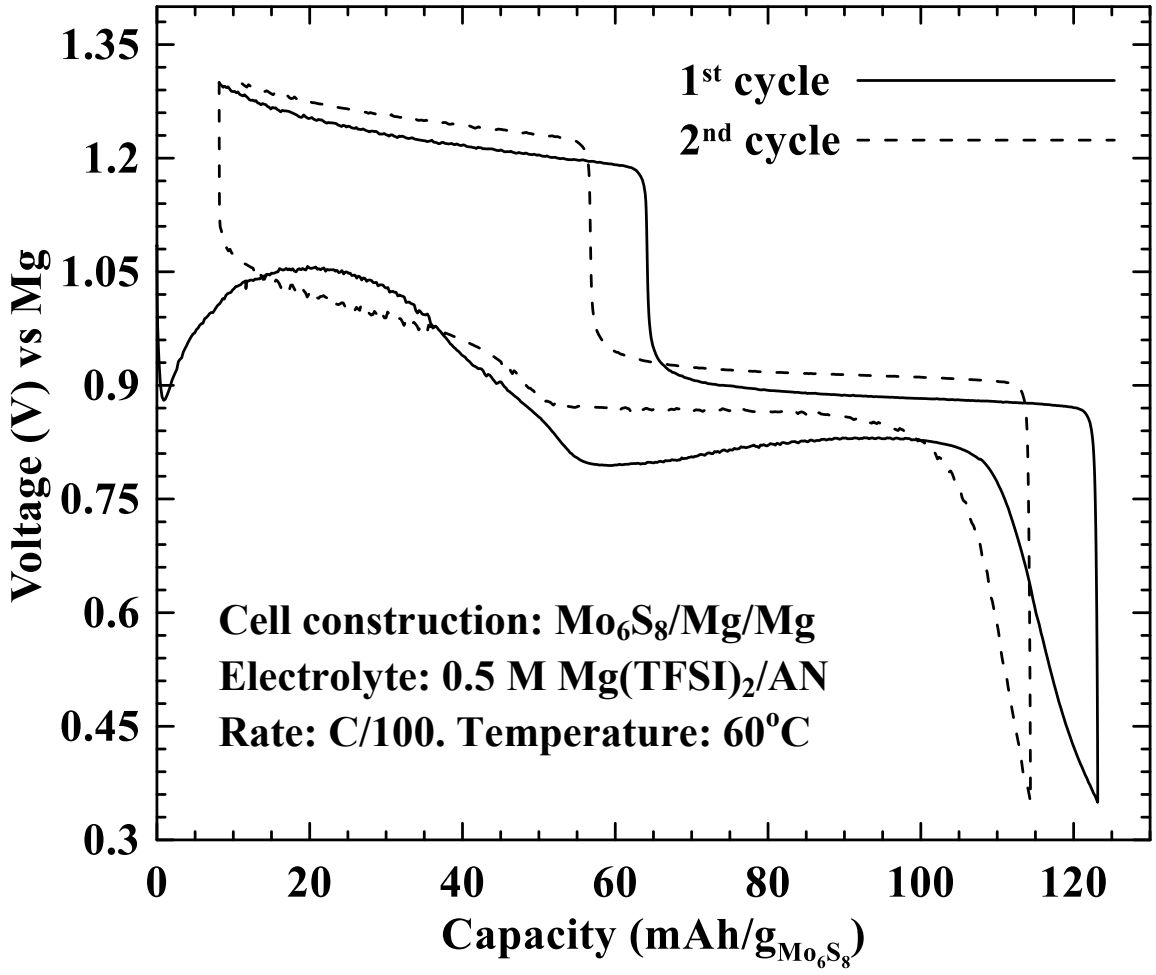

Figure 19 – Voltage profile of a Mo_6S_8/Mg/Mg three electrode cell with 0.5M $Mg(TFSI)_2$/AN electrolyte operated at 60°C.

3.4 Conclusions

$Mg(TFSI)_2$/AN was evaluated as an electrolyte for use in magnesium electrochemistry. This electrolyte was oxidatively stable up to 2.8 V against stainless steel. At higher voltages stainless steel corrosion occurred. At low voltages, $Mg(TFSI)_2$/AN electrolyte was observed to reductively decompose against stainless steel to as low as -0.2 V vs. Mg. This reaction can mimic Mg plating, however no evidence of Mg plating was observed. Therefore, even 3-electrode cells that appear to cycle reversibly in this electrolyte may actually be decomposing acetonitrile during each

reductive half-cycle at the counter electrode. Researchers need to be aware of the possibility of solvent reduction, which may appear to be Mg plating or insertion. This brings into question earlier reports in of reversible cycling behaviour of Mg insertion in alloys in this electrolyte.

At more oxidizing voltages, reversible electrochemistry was demonstrated in $Mg(TFSI)_2$/AN electrolyte. Chevrel phase Mo_6S_8 was reversibly magnesiated and de-magnesiated in this electrolyte at a greater capacity than occurred in Grignard solvent and with significantly less irreversible capacity. Results from this study show that $Mg(TFSI)_2$/AN electrolyte may be used in Mg-ion full cells in which the anode is kept sufficiently high voltage to avoid electrolyte reduction. This may present a practical alternative to the use of Grignard-based electrolytes. Further studies are needed to measure the conductivity of this electrolyte system, to verify that it sufficient for practical cells.

CHAPTER 4
ALTERNATIVE COUNTER/REFERENCE/NEGATIVE ELECTRODE FOR MAGNESIUM-BASED BATTERIES

4.1 Introduction

As mentioned previously, conventional battery electrolytes using alkyl carbonates and acetonitrile solvents form a thick passivation layer on Mg metal, making Mg deposition impossible [44]. Additionally, according to the study shown in chapter 3, the reduction of electrolyte at low potential toward cell's hardware may lead to misleading results. Therefore, it is in need for the development of a better counter/reference electrode to use in Mg-based batteries research, as well as a better negative electrode for full practical Mg-ion cells.

There are several requirements that the candidates for the better counter/reference/negative electrode must satisfy. For a better counter/reference electrode, the potential of the candidate materials, while the cell is cycling, must be well-known. Therefore it is desirable that the voltage of the electrode be independent of Mg composition.

Mg-Bi [54], Mg-Sb [55] and Mg-Pb [56] phase diagrams predict that these systems should have simple voltage curves with a single plateau corresponding to a two phase region between the host element and the single alloy phase in these systems (forming Mg_3Bi_2, Mg_3Sb_2 and Mg_2Pb). In fact, single plateau potential curves have been observed when Mg is alloyed with Bi and Sb electrochemically [18]. Using the same method described on Chapter 2 to calculate the potential of these alloy systems results in

the potentials of Mg_3Bi_2, Mg_3Sb_2 and Mg_2Pb as 0.35 V, 0.62 V and 0.10 V vs. Mg, respectively. The low constant voltage of these materials versus magnesium makes them attractive for use as anodes in magnesium cells and also for counter/reference/negative electrodes for Mg-based battery research and development. Here an examination of the Mg-Pb system will be discussed.

4.2 Experimental

Pb electrodes were prepared by cutting stainless steel (SS) foils into electrode disks. These SS disks were weighed using a Satorius SE-2 microbalance (±0.1 μg resolution). Pb was sputtered deposited on the SS foil using a modified Corona Vacuum Coater V-3T deposition system. Details of this sputtering system have been described in reference [57]. A base pressure of 7.6×10^{-7} Torr with a 3.1 mTorr argon pressure and a 35W target power were used during the deposition process. After sputtering, electrodes were immediately transferred into an Ar-filled glovebox for storage to minimize the oxidation of Pb. The amount of Pb on the SS disk was determined as the mass difference between the SS disk prior to and after the sputtering process.

In this study, Grignard-based AEC in THF was used as electrolyte. AEC was made by diluting 2 M EtMgCl in THF solution (Sigma Aldrich) with THF (Sigma Aldrich, anhydrous, 99.9%) to obtain 0.5 M EtMgCl in THF solution. Then, an amount of $AlCl_3$ powder (Alfa Aesar, anhydrous, 99.985%) was added into this solution to obtain 2:1 EtMgCl/$AlCl_3$ by mole. This electrolyte was stirred for 24 hours before use.

2-electrode coin cells were constructed as described in section 3.2. Electrochemical testing was performed using a Maccor Series 4000 Automated Test

System. XRD measurement of the magnesiated Pb that was harvested from a coin cell was done according to the same method as described in section 3.2.

The morphology of the electrodes was obtained using a Hitachi S-4700 scanning electron microscopy (SEM) system. Cell used for SEM study was disassembled in an Ar-filled glovebox after cycling. The cycled electrode was then rinsed with THF and dried under vacuum. This electrode was kept in an air-tight, Ar-filled vial until mounted into SEM holder to minimize any possible oxidation. The morphology of this electrode was taken using secondary electron mode.

4.3 Results

Based on the theoretical treatment of alloy materials in Chapter 2, Pb-Mg alloy should have a maximum theoretical capacity of 517 mAh/g (corresponding to the formation of Mg_2Pb) with a volume expansion of 153%. Figure 20 shows magnesiation and de-magnesiation of Pb at 60^{o}C at a rate of C/50. The Pb film was sputtered so that its thickness was about 1.9 μm. One plateau corresponding to Mg_2Pb formation is noted as expected from the binary phase diagram of the Mg-Pb system. In the 1st cycle (not shown), only 0.2% of the theoretical capacity was reached. This indicates that Mg can only diffuse a short distance into Pb. According to the capacity obtained during the first cycle, this distance corresponds to approximately 0.2 μm. In the following cycles, progressive magnesiation of the sputtered Pb electrode with cycle number was observed. It is speculated that the increase in capacity may be attributed to the progressive exposure of more pristine Pb metal as the electrode surface undergoes cracking due to volume reduction during de-magnesiation. After the 4th cycle (not shown), the capacity fades to

zero capacity. This behaviour may due to the large volume change that occurs when Pb is cycled, leading to fracture of the surface and electrically disconnected Pb particles.

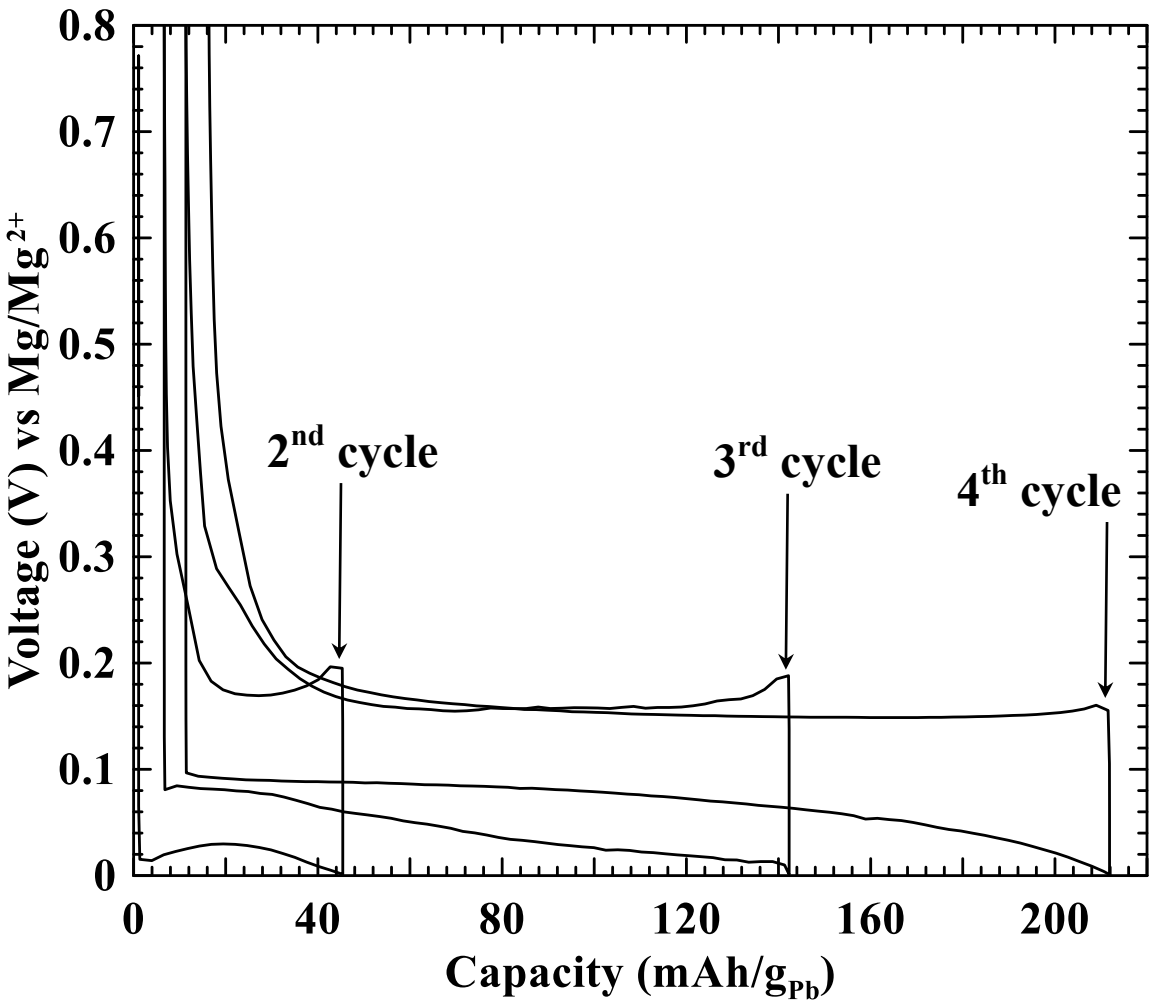

Figure 20 – Voltage profile of a Pb/Mg coin cell operated at 60°C. This cell was cycling at C/50 rate.

Figure 21 shows the morphology of the pristine Pb electrode and the cycled electrode. The surface of cycle electrode shows higher porosity compared to the pristine Pb electrode. This indicates that the magnesiation process of Pb leads to the fracture of the surface. In order to understand in more detail the diffusion mechanism of Mg^{2+} into Pb, more detailed SEM studies of the electrodes including the cross section of the electrodes should be performed.

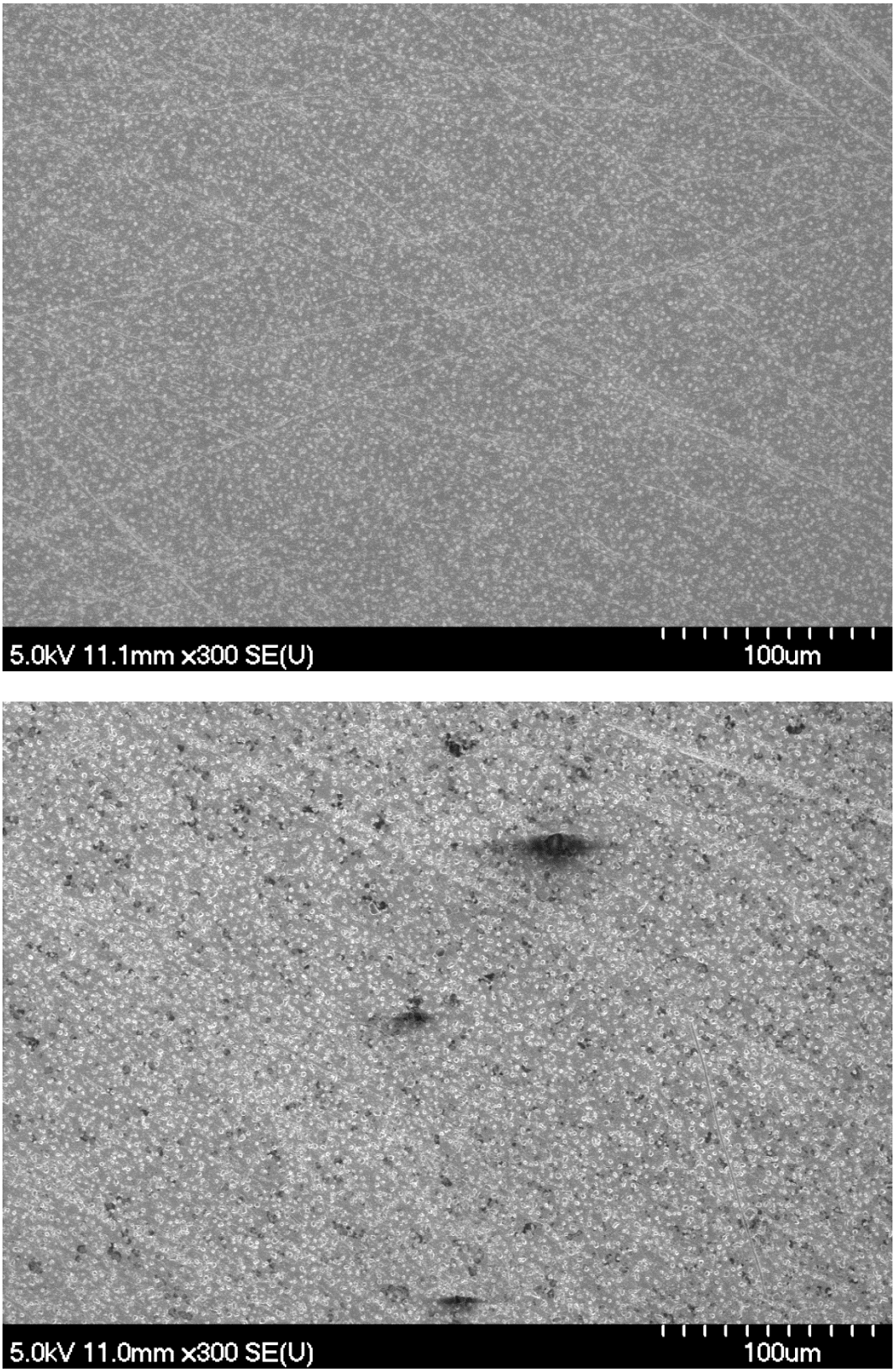

Figure 21 – SEM of pristine Pb electrode (top) and Pb electrode after cycled (bottom).

Due to the high vapor pressure and low boiling point of THF, coin cell performance at 60°C is difficult to reproduce. Under high internal pressure caused by THF vapor at these temperatures, the coin cell tends to break open. In order to prevent this, subsequent coin cells were operated at 30°C, although the kinetics of Mg insertion are much slower at this temperature.

Figure 22 shows the first 1.5 cycles of a Pb vs. Mg coin cell that was operated at 30°C. This cell was cycled at a much slower rate, C/100, in order to achieve the highest possible capacity. In addition, the Pb sputtered layer was made much thinner (0.44 μm) than the previous film, so that the Mg diffusion distance would be smaller. As a result the about 89% of the Pb film was magnesiated during the first cycle. An XRD measurement of the magnesiated Pb electrode from this cell is shown in Figure 23. The presence of Pb peaks and Mg_2Pb peaks show that the insertion of Mg into Pb is incomplete, which is consistent with electrochemical results.

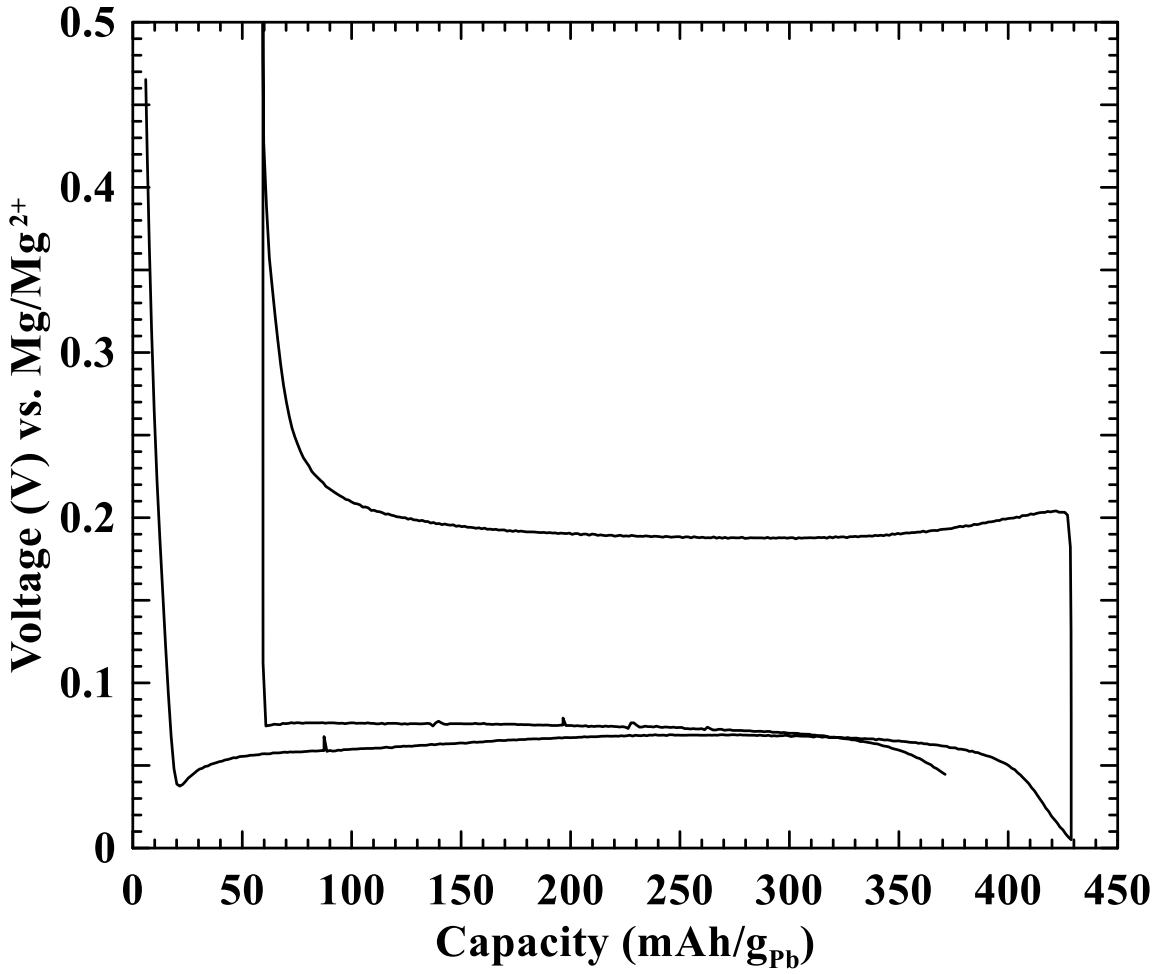

Figure 22 – Voltage profile of a Pb/Mg coin cell at 30°C and C/100.

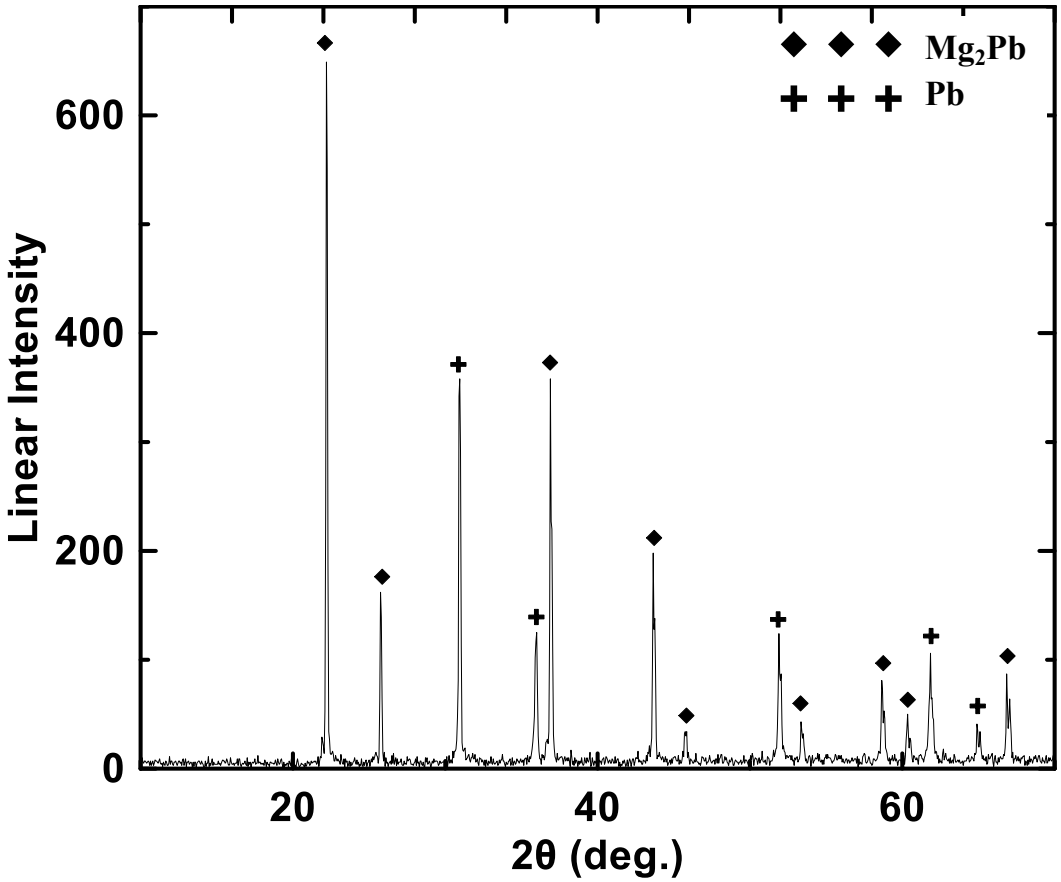

Figure 23 – XRD measurement of the magnesiated Pb electrode. The diamond and the cross indicate peak positions from Mg_2Pb (PDF 00-065-2998) and Pb (PDF 00-004-0686), respectively [25].

4.4 Conclusions

In this chapter, reversible cycling of a Pb vs. Mg cell has been shown. It is speculated that as the Pb film is magnesiated it becomes fractured and porous, allowing for progressively deeper magnesiation after each cycle, leading to increasing capacity. However the fracture of the film eventually causes the capacity to fade due to electrically disconnected portions of the electrode. To confirm this concept further studies, such as SEM imagery of the cycled electrode's cross section, are needed.

CHAPTER 5
DEVELOPMENT OF NEW CELL HARDWARE

5.1 Introduction

As seen in chapter 3, the use of Mg metal as the counter electrode for the study of new electrolyte systems for Mg-based batteries could lead to misleading results due to the reduction of electrolyte at low voltage. Therefore, it is vitally important to use 3-electrode cells while doing research of materials and electrolyte research for Mg-based batteries. However, 3-electrode coin cells were often found to leak, mostly due to interactions between the electrolyte and Torr Seal. Torr Seal requires thirty minutes to several hours to be fully cured. During this time, the pressure built-up from the evaporation of electrolyte may cause the Torr Seal to rupture and result in a cell leak. In addition, as mentioned in chapter 4, under pressure built-up from the evaporation of electrolyte at high operating temperature, the traditional 2-electrode coin cell hardware can hardly withstand these internal pressures. To overcome these problems, more rigid cell hardware has been developed.

5.2 Experimental

Figure 24 shows the schematic structure of the newly design cell hardware. Three Conflat® vacuum flanges are bolted together using non-conductive bolts (only the bolt holes are shown in the figure). Polyimide tape is placed between Conflats® to prevent electrical contact. High-density polyethylene (HDPE) washers are also placed between the Conflat® flanges as gaskets in order to seal the cell, while keeping the Conflats® electrically insulated from each other. The stack pressure of the cell is controlled by a

carbon-steel spring. In this structure, the top spacer and the bottom spacer are in contact with the top Conflat® flange and the bottom Conflat® flange, respectively.

When used as a 2-electrode cell, the counter electrode is placed at the bottom of the top spacer. Both the top spacer and the counter electrode are contained inside a HDPE cylinder to prevent electrical contact with the middle Conflat® piece. Similarly, the bottom spacer with the working electrode that is placed on top is contained inside another HDPE cylinder. These electrodes are separated by Celgard® and BMF separators as in a normal 2-electrode coin cell. When used as a 3-electrode cell, an additional ring shaped reference electrode is placed on top of a SS ring current collector, which has a tab to make electrical contact to the middle Conflat® flange. The reference electrode is sandwiched between the cell separators, so that it does not come into electrical contact with either the working or counter electrode.

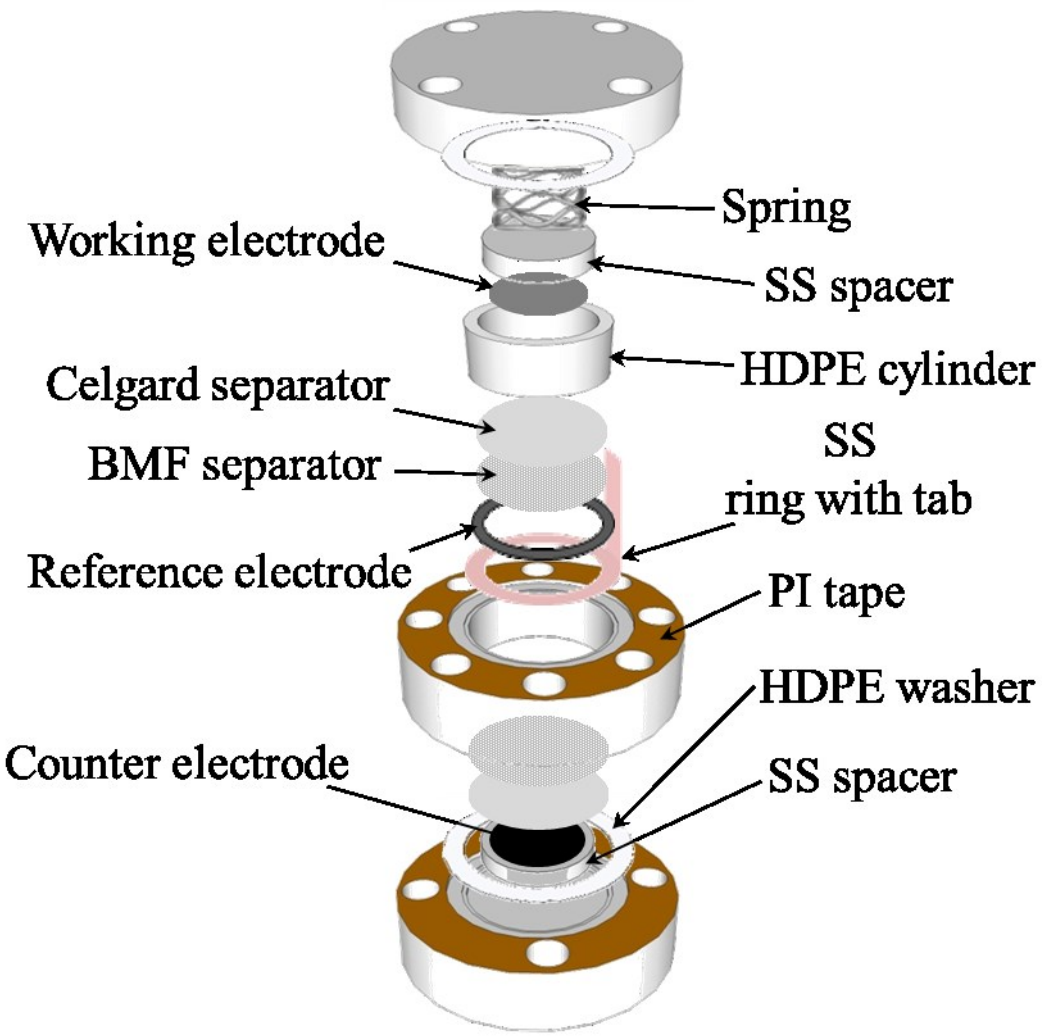

Figure 24 – Schematic structure of a Conflat® cell

The electrodes which were used to evaluate this cell hardware were: Mo_6S_8 electrodes, prepared as described in section 3.2.; and mesocarbon microbeads (MCMB) electrodes, prepared using the same method as the Mo_6S_8 electrodes to obtain 80/10/10 of MCMB, carbon black and PVDF by weight. The lithium nickel manganese cobalt oxide (NMC) cathodes and graphite anodes (matched electrode coatings provided by 3M Company) were used to test full cells. .

Electrolytes were: 0.5 M EtMgCl in THF (2:1 EtMgCl:$AlCl_3$ by mole) for Mg-based cells, prepared as described in section 4.2 and 1M $LiPF_6$ in 1:2 EC:DEC by volume for Li-based cells.

5.3 Results

Consistent with the nomenclature of Chapter 3, cells will be described here according to their electrode composition with the nomenclature: working/reference/counter. Figure 25 shows the 5th cycle of a NMC/Li/Graphite full cell with a lithium reference electrode that was constructed using a Conflat® cell. Compared to a coin cell that used identical electrodes and electrolyte (Figure 26), the voltage profile of the Conflat® cell shows larger polarization between charge and discharge curves. As can be seen in the voltage curve of the cathode vs. the reference electrode, the cell polarization is mainly from the NMC electrode. The reason for this behaviour might be due to insufficient stack pressure in the Conflat® cell.

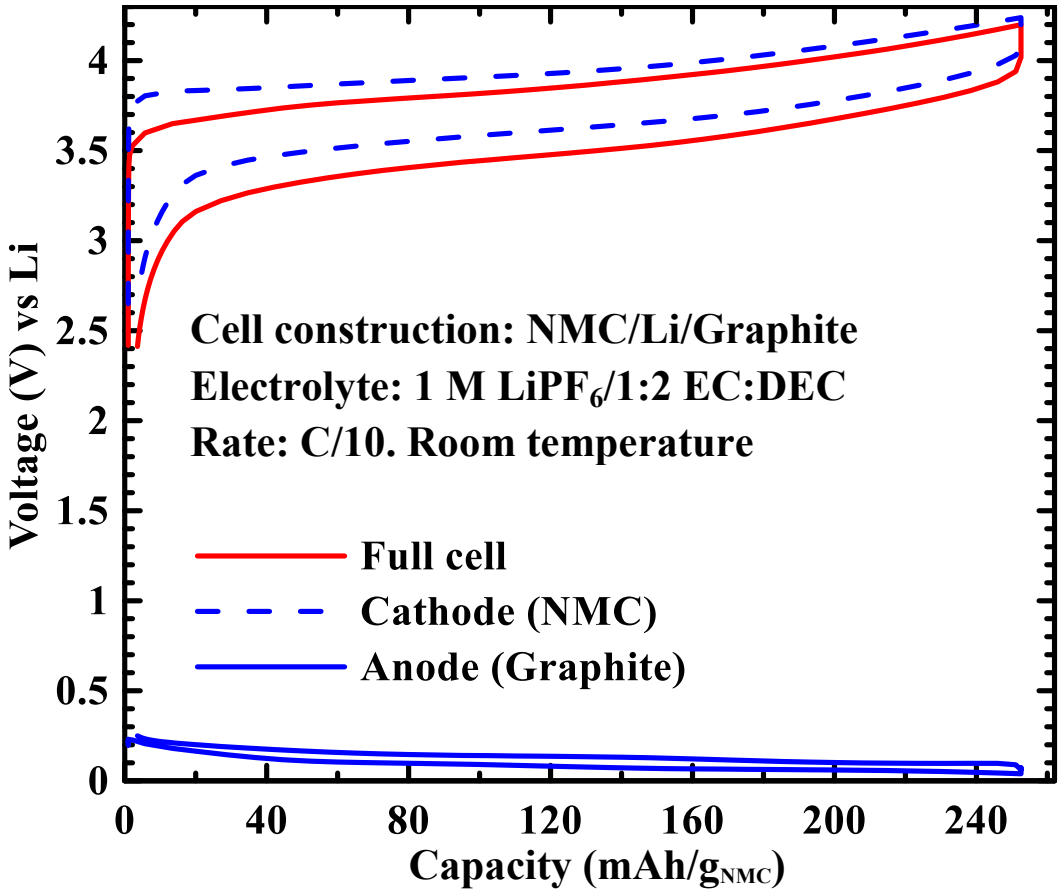

Figure 25 – Voltage profile of 5th cycle of a NMC/Li/Graphite Conflat® cell

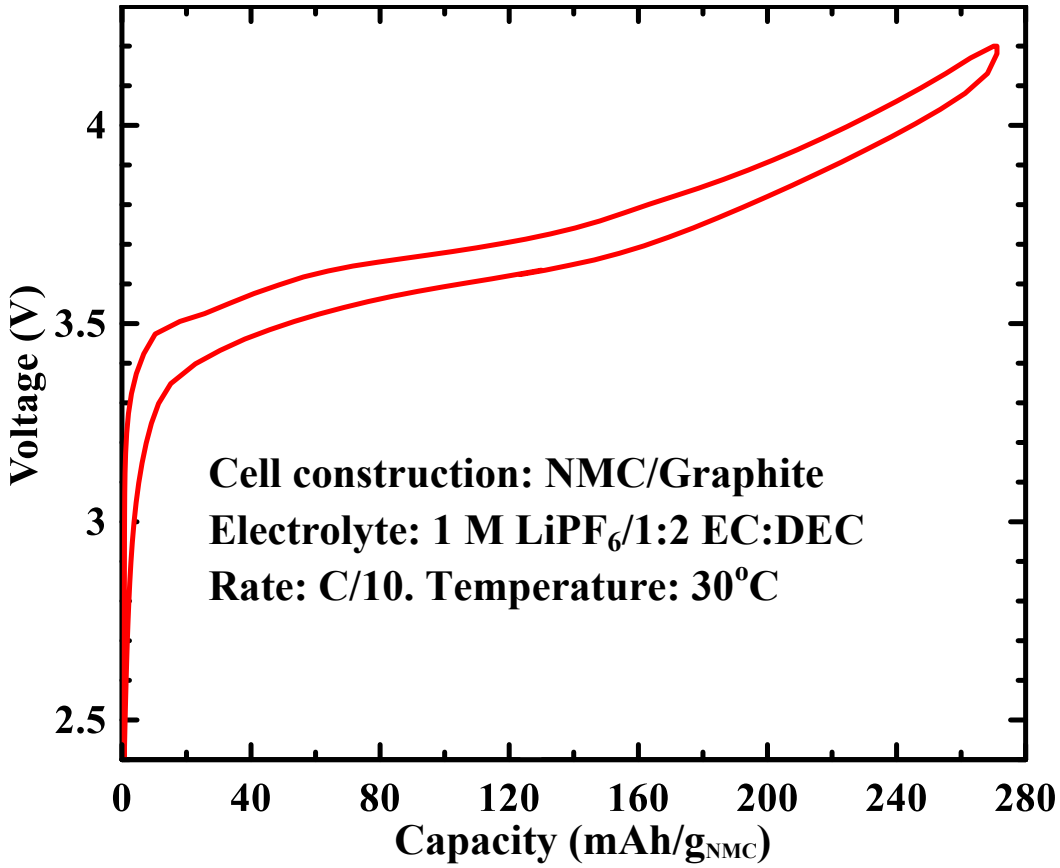

Figure 26 – Voltage profile of 5th cycle of a NMC/Graphite coin cell.

To increase stack pressure in the cell, thicker SS spacers were used. Figure 27 shows the voltage profile of a NMC/Li/Graphite Conflat® cell using thicker SS spacers. Compared to the result from Figure 25, the polarization has been decreased significantly. However, when this cell was opened after 10 cycles, the spring was broken. This might be due to the pressure being higher than the loading capacity of the spring. Based on these results, a higher loading spring is being obtained to improve the Conflat® cell performance.

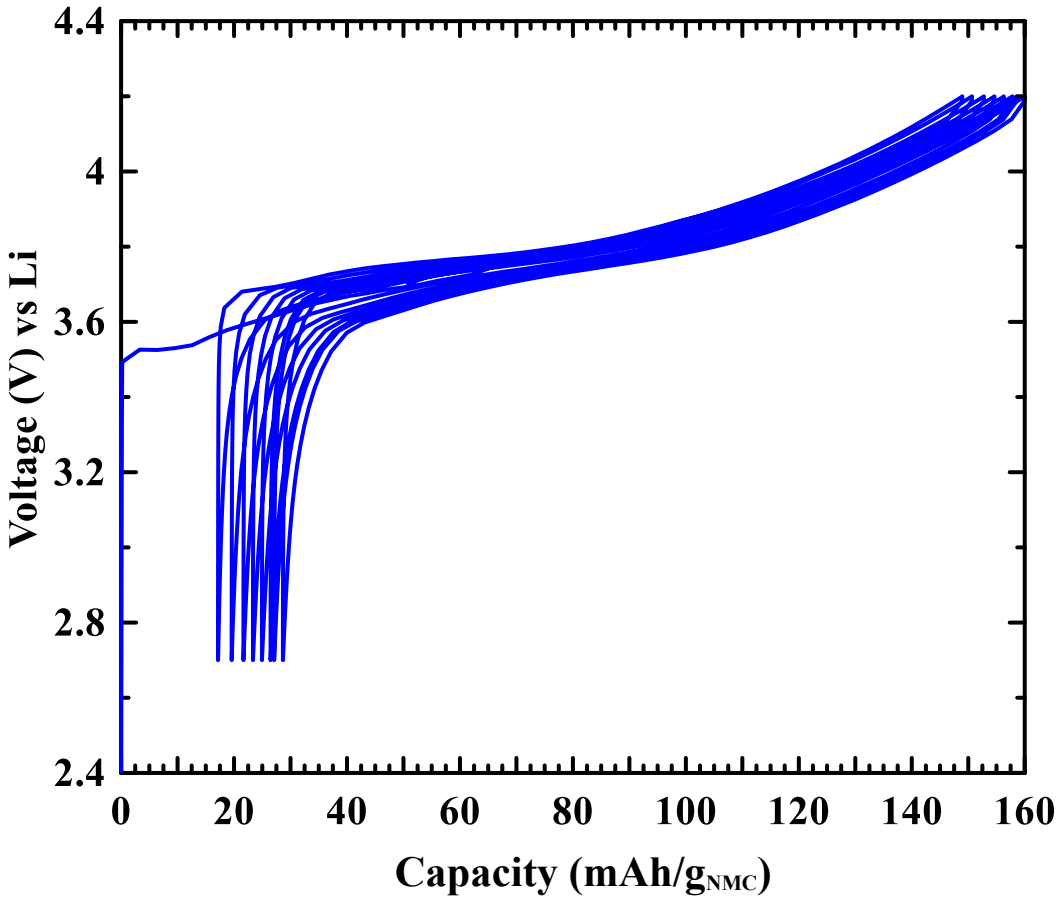

Figure 27 – Voltage profile of a NMC/Li/Graphite Conflat® cell using thicker SS spacers.

Figure 28 shows the voltage curve of a Mo_6S_8/Mg/Mg cell operated at 30°C. It is not fully understood why the stripping of the Mg counter electrode is measured to occur below 0 V. However, similar to the case of Mo_6S_8/Mg/Mg cell using $Mg(TFSI)_2$/AN electrolyte (section 3.3), both plateaus from the voltage curve of the Mo_6S_8 working electrode are shifted down equally compared to the case of Mo_6S_8/Mg cell using AEC/THF electrolyte. It, again, is possible that the shift comes from the Mg reference electrode.

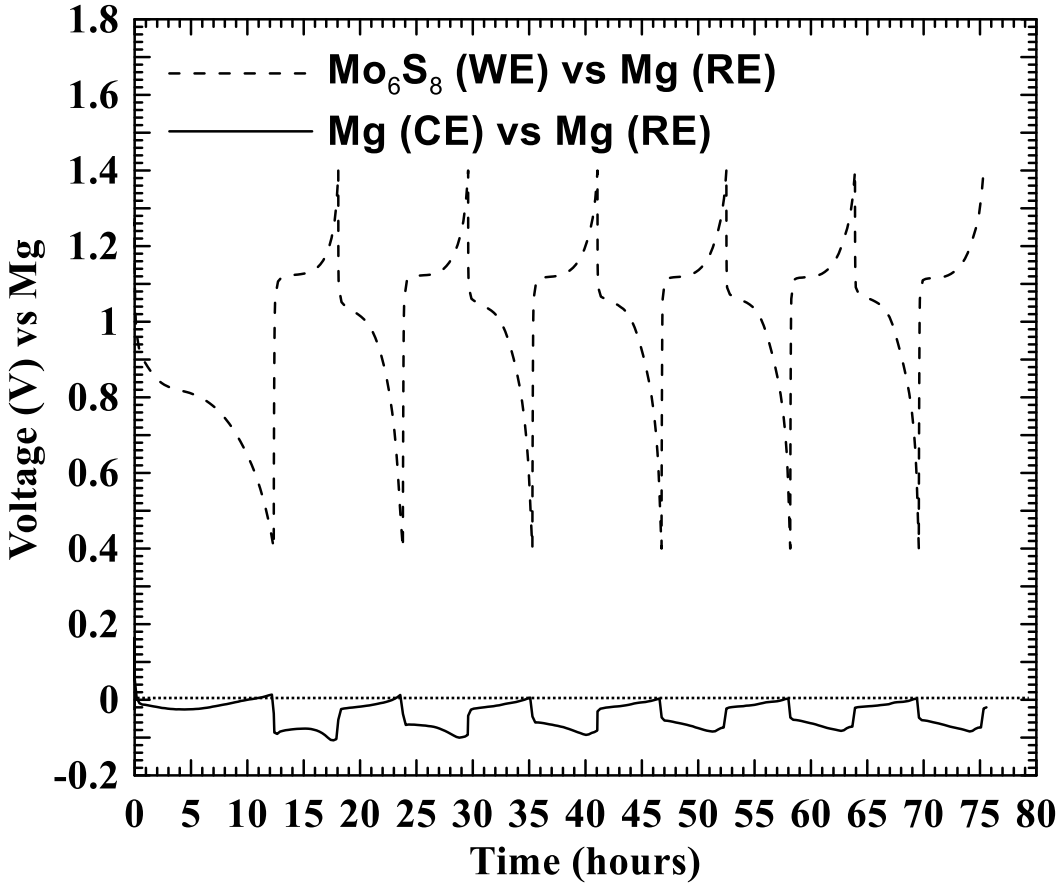

Figure 28 – Voltage profile of a Mo_6S_8/Mg/Mg Conflat® cell using 0.5M EtMgCl in THF (2:1 EtMgCl:$AlCl_3$ by mole) electrolyte at 30°C. Rate: C/12.5.

5.4 Conclusions

Based on initial results, the Conflat® cell design has proven to be easily assembled, not leak, even at elevated temperatures, and produce results consistent with coin cell hardware. The use of higher temperature gaskets and cell hardware to replace polyethylene (e.g. with Teflon or boron nitride) should allow the Conflat® cell to operate at temperatures of 200°C or beyond.

CHAPTER 6
CONCLUSIONS

In this thesis, the volume expansion behavior and volumetric energy densities of metal alloy negative electrodes (A_xM) for metal-ion batteries based on A = Li, Na, K, Mg, Ca and Al were compared. It was found that each metal ion, A, occupies a characteristic volume in alloys which is almost insensitive to the host metal, M. All alloy systems, with the exception of K-Sn and Na-Sn systems, were found to have similar or greater volumetric energy density than conventional graphitic anodes in Li-ion cells. It is predicted that both the Mg_xM and Al_xM systems might achieve higher energy densities than possible with any Li-ion negative electrode known and operate at potentials at which organic electrolytes are known to be stable.

Mg battery research has almost exclusively used Grignard reagents for electrolytes. Due to the limitations of Grignards electrolytes, researchers have been looking for a more oxidative stable, lower vapor pressure and less toxic electrolytes to enable practical Mg-based batteries. According to this study, $Mg[N(SO_2CF_3)_2]_2$/AN electrolyte was found to have a stable potential range up to 2.8 V vs. Mg against a stainless steel working electrode. Using this electrolyte, no Mg plating was observed. Reversible intercalation of Mg into Mo_6S_8 was demonstrated in this electrolyte with significantly lower irreversible capacity, compared to cycling in Grignard-based electrolytes. However, operating at lower voltages resulted in acetonitrile reduction. Therefore, $Mg[N(SO_2CF_3)_2]_2$/AN electrolyte may be useful for Mg-ion batteries, if the negative electrode has sufficiently high voltage to avoid acetonitrile reduction.

To avoid the reduction of acetonitrile, magnesiated Pb appears to be a good candidate to replace Mg metal as the counter/reference/negative electrode in Mg-based battery research. The potential 0.1 V vs. Mg of magnesiated Pb in Grignard-based reagents might be high enough to avoid the reduction of acetonitrile when used in $Mg(TFSI)_2$/AN electrolyte. Similar experiments as conducted with Pb in Grignard reagent electrolyte should be repeated using $Mg(TFSI)_2$/AN electrolyte to confirm if Mg can be inserted into Pb using an acetonitrile solvent. Pb also shows promise as a negative electrode in Mg-ion batteries. However, there are still many aspects that need to be studied in more detail including the effect of electrolytes, electrolyte's additives and operating temperature on the diffusion rate of Mg into Pb. Future studies might also include possible active/inactive electrode systems to minimize capacity loss due to alloy fracture in 2-phase regions. Making the Pb phase nano-structured might also be advantageous as it would reduce the Mg diffusion path length.

The development of the Conflat® cell provides a unique opportunity to evaluate the characteristics of electrolyte compositions in 3-electrode cells that are quick and simple to assemble. The initial design phase is almost complete, resulting in performance similar to that obtained in coin cells. Some adjustments are required to bring the operating temperature of this design to at least 200^{o}C. Also, some small adjustments on spacers' thickness and spring's loading are required in order to obtain acceptable stack pressure.

REFERENCES

[1] K. Brandt, *Solid State Ionics*, **69** (1994) 173.

[2] H. Inoue, *Proceedings IMLB*, (2006) 0228.

[3] C. Delmas, J.-J. Braconnier, C. Fouassier, and P. Hagenmuller, *Solid State Ionics*, **3/4** (1981) 165.

[4] D.A. Stevens and J.R. Dahn, *J. Electrochem. Soc.*, **147** (2000) 1271.

[5] B.L. Ellis, W.R.M. Makahnouk, Y. Makimura, K. Toghill, and L.F. Nazar, *Nature Materials*, **6** (2007) 749.

[6] S. Komaba, C. Takei, T. Nakayama, A. Ogata, N. Yabuuchi, *Electrochem. Comm.*, **12** (2010) 355.

[7] P. Novák, R. Imhof, and O. Haas, *Electrochim. Acta*, **45** (1999) 351.

[8] D. Aurbach, H. Gizbar, A. Schechter, O. Chusid, H.E. Gottlieb, Y. Gofer, and I. Goldberg, *J. Electrochem. Soc.*, **149** (2002) A115.

[9] M.N. Obrovac, L. Christensen, D.B. Le, and J.R. Dahn, *J. Electrochem. Soc.*, **154** (2007) A849.

[10] R. Chevrel, M. Sergent and K. Prigent, *J. Solid State Chem.*, **3** (1971) 515.

[11] P. Jolieois, *Compt. Rend.*, **155** (1912) 353.

[12] T.S. Arthur, N. Singh, and M. Matsui, *Electrochem. Commun.*, **16** (2012) 103.

[13] M.N. Obrovac and L. Christensen, Electrochem. *Solid-State Lett.*, **7** (2004) A93.

[14] *Binary Alloy Phase Diagrams*; 2nd ed.; T.B. Massalski Ed.; ASM International: Materials Park, OH, 1990; **vol. 3**, p.2468.

[15] *Binary Alloy Phase Diagrams*; 2nd ed.; T.B. Massalski Ed.; ASM International: Materials Park, OH, 1990; **vol. 1**, p.953.

[16] *Binary Alloy Phase Diagrams*; 2nd ed.; T.B. Massalski Ed.; ASM International: Materials Park, OH, 1990; **vol. 3**, p.2548.

[17] *JCPDS International Centre for Diffraction Data*, PDF-2, Release 2002.

[18] *Binary Alloy Phase Diagrams*; 2nd ed.; T.B. Massalski Ed.; ASM International: Materials Park, OH, 1990; **vol. 3**, p.2470.

[19] *Binary Alloy Phase Diagrams*; 2nd ed.; T.B. Massalski Ed.; ASM International: Materials Park, OH, 1990; **vol. 3**, p.2734.

[20] *Binary Alloy Phase Diagrams*; 2nd ed.; T.B. Massalski Ed.; ASM International: Materials Park, OH, 1990; **vol. 3**, p.2389.

[21] *Binary Alloy Phase Diagrams*; 2nd ed.; T.B. Massalski Ed.; ASM International: Materials Park, OH, 1990; **vol. 1**, p.955.

[22] *Binary Alloy Phase Diagrams*; 2nd ed.; T.B. Massalski Ed.; ASM International: Materials Park, OH, 1990; **vol. 3**, p.2551.

[23] *Binary Alloy Phase Diagrams*; 2nd ed.; T.B. Massalski Ed.; ASM International: Materials Park, OH, 1990; **vol. 1**, p.168.

[24] *Binary Alloy Phase Diagrams*; 2nd ed.; T.B. Massalski Ed.; ASM International: Materials Park, OH, 1990; **vol. 1**, p.132.

[25] *Binary Alloy Phase Diagrams*; 2nd ed.; T.B. Massalski Ed.; ASM International: Materials Park, OH, 1990; **vol. 1**, p.170.

[26] *Binary Alloy Phase Diagrams*; 2nd ed.; T.B. Massalski Ed.; ASM International: Materials Park, OH, 1990; **vol. 1**, p.142.

[27] *Binary Alloy Phase Diagrams*; 2nd ed.; T.B. Massalski Ed.; ASM International: Materials Park, OH, 1990; **vol. 1**, p.148.

[28] *Binary Alloy Phase Diagrams*; 2nd ed.; T.B. Massalski Ed.; ASM International: Materials Park, OH, 1990; **vol. 1**, p.226.

[29] *Binary Alloy Phase Diagrams*; 2nd ed.; T.B. Massalski Ed.; ASM International: Materials Park, OH, 1990; **vol. 1**, p.172.

[30] D. Howell, *Progress Report for Energy Storage Research and Development, U.S.*

[31] A. Manthiram, *J. Phys. Chem. Lett.*, **2** (2011) 176.

[32] S. Komaba, T. Nakayama, A. Ogata, T. Shimizu, C. Takei, S. Takada, A. Hokura, and I. Nakai, *ECS Transactions*, **16** (2009) 43.

[33] Materials Project, *http://www.materialsproject.org/*, **accessed Oct. 30, 2012.**

[34] A. Jain, G. Hautier, C.J. Moore, S.P. Ong, C.C. Fischer, T. Mueller, K.A. Persson, and G. Ceder, *Comput. Mater. Sci.*, **50** (2011) 2295.

[35] *Handbook of Chemistry and Physics: 88th Edition*, CRC Press (2007)..

[36] Z. Lu, A. Schechter, M. Moshkovich, and D. Aurbach, *J. Electroanal. Chem.*, **466** (1999) 203.

[37] N. Pour, Y. Gofer, D.T. Major, and D. Aurbach, *J. Amer. Chem. Soc.*, **133** (2011) 6270.

[38] J. Muldoon, C.B. Bucur, A.G. Oliver, T. Sugimoto, M. Matsui, H.S. Kim, G.D. Allred, J. Zajicek, and Y. Kotani, *Energy Environ. Sci.*, **5** (2012) 5941.

[39] E. Levi, Y. Gofer, Y. Vestfreed, E. Lancry and D. Aurbach, *Chem. Mater.*, **14** (2002) 2767.

[40] A. Mitelman, M.D. Levi, E. Lancry, E. Levi and D. Aurbach, *Chem. Commun.*, (2007) 4214.

[41] E. Lancry, E. Levi, Y. Gofer, M. Levi, G. Salitra, and D. Aurbach, *Chem. Mater.*, **16** (2004) 2832.

[42] S. Kondo and K. Takada, *Solid State Ionics*, **57** (1992) 147.

[43] R.A. Dunlap, D.A. Small, D.D. MacNeil, M.N. Obrovac and J.R. Dahn, *J. Alloys Compd.*, **289** (1999) 135.

[44] *Binary Alloy Phase Diagrams*; 2nd ed.; T.B. Massalski Ed.; ASM International: Materials Park, OH, 1990; **vol. 1**, p.760.

[45] *Binary Alloy Phase Diagrams*; 2nd ed.; T.B. Massalski Ed.; ASM International: Materials Park, OH, 1990; **vol. 3**, p.2544.

[46] *Binary Alloy Phase Diagrams; 2nd ed.*; T.B. Massalski Ed.; ASM International: Materials Park, OH, 1990; **vol. 3**, p.2534.

[47] J.R. Dahn, S. Trussler, T.D. Hatchard, A. Bonakdarpour, J.R. Mueller-Neuhaus, K.C. Kewitt, and M. Fleischauer, *Chem. Mater.*, **14** (2002) 3519.

[48] L.J. Krause, W. Lamanna, J. Summerfield, M. Engle, G. Korba, R. Loch, R. Atanasoski, *J. Power Sources*, **68** (1997) 320.

[49] Jing Li and J.R. Dahn, *J. Electrochem. Soc*, **153** (2007) A156.

[50] D.A. Kramer, Magnesium, *http://minerals.usgs.gov/minerals/pubs/commodity/magnesium/400798.pdf*, **accessed Nov. 30, 2012**.

[51] J.A. Ober, Lithium, *http://minerals.usgs.gov/minerals/pubs/commodity/lithium/450798.pdf*, **accessed Nov. 30, 2012**.

[52] ESU-services Ltd., *http://www.esu-services.ch/index.php?id=106*, **accessed Nov. 30, 2012**.

[53] S. Ramakrishnan and P. Koltun, *Magnesium Technology 2004*, (2004) 173.

[54] A. Stamp, D.J. Lang, and P.A. Wager, *J. Cleaner Production*, **23** (2012) 104,.

[55] K. Yvon, in *Current Topics in Material Science*, **vol. 3**, E. Kaldis, Editor, p. 62, North-Holland Publishing Company, Amsterdam (1979).

[56] D.A. Kramer, *http://minerals.usgs.gov/minerals/pubs/commodity/magnesium/mcs-2011-mgmet.pdf*, **accessed Nov. 30, 2012**.

[57] R. Chevrel, M. Sergent and K. Prigent, *Mat. Res. Bull.*, **9** (1974) 1487.